Abstract

Fuel cells with solid oxide electrolytes (SOFCs) have attracted increasing interest as efficient alternatives to combustion-based energy production. Doped perovskites have displayed mechanical stability and high proton conductivity in the key 500-700℃ temperature range, making investigation of proton conduction in perovskites an important step in the fuel cell development process. This work details the characterization of a perovskite grain boundary expected to display unique conduction behavior, the fine-tuning and testing of a new multistep Kinetic Monte Carlo (KMC) algorithm for generating long-range conduction pathways, and the application of a graph theoretical centrality measure to help explain system-specific conduction patterns.

Although proton conduction in bulk perovskites is well understood, many questions remain about proton conduction in grain boundaries, which represent major barriers to conduction. Theoretical study a grain boundary system begins with full energetic characterization of conduction in the system. As a first step in this process, optimum energies for Y/$BaZrO_3$ (310) tilt grain boundaries doped at different sites have been calculated using density functional theory. Results from different exchange correlation functionals have been compared.

Because proton conduction in perovskite systems involves a series of rare proton movements, it can be modeled with KMC simulations. The standard KMC

algorithm involves moving a proton between binding sites, using random numbers and rate constants to pick moves in proportion with their probability. We have modified this algorithm to generate n-step pathways from each site. At each iteration, a pathway rather than a single move is selected. Results for the $Y/BaZrO_3$, $Al/BaZrO_3$, $Y/SrZrO_3$, and $Al/SrZrO_3$ systems have been in good agreement with standard KMC results, showing that probable pathways run through different regions in systems with different dopants. A valid method of calculating rate constants for multi-step moves has been developed, and the multi-step algorithm has been shown to increase computational efficiency.

Graph theoretical methods have been applied to provide additional insight into the relationships between binding sites. Average hitting time between sites has been used to rank binding sites based on accessibility. The contrasting patterns of rankings in each system are consistent with contrasting trends in conduction pathways and barriers, suggesting that graph theoretical ranking may prove a quick, powerful tool for predicting conduction trends in perovskite systems.

Thus, this work refines an existing technique for generating proton conduction pathways, applies a graph theoretical centrality measure to proton conductors for the first time, and begins the characterization of a grain boundary system, the first step toward full analysis of conduction trends.

Determining and Understanding Long-Range Proton Conduction Pathways and Patterns in Perovskite Systems

A thesis presented to the faculty
in partial fulfillment of the requirements for
the degree of bachelor of arts in the subject of
chemistry

by Rachel A. Krueger

Mount Holyoke College
South Hadley, Massachusetts
2013

Acknowledgments

I would like to use this space to thank everyone who has made sure that my chemical career at Mount Holyoke went forward during the past three years. If Kathryn Krueger had not called it very early on and convinced me that general chemistry would change my life, or if Desiree Plata had not taught a course capable of changing my life, I would never have begun the task. I am indebted to all of the professors in the chemistry department (and a few in philosophy and mathematics) for the excellent advice I've consistently received. In particular, I am grateful to my thesis committee members, Margaret Robinson and Wei Chen. It has been a privilege to spend two years in the Gomez Group and receive Maria Gomez's exceptional guidance and instruction. The first time I stepped into her office was the moment I jumped into the great intellectual and moral machine that is Mount Holyoke. None of my work would have been possible without my parents' generous and cheerful support, and it makes me happy to think sometimes that they have become almost as enthusiastic about fuel cells as I have.

The computational and financial support provided by MERCURY, Mount Holyoke College, and the National Science Foundation is gratefully acknowledged. Finally, I am grateful to my fellow Mount Holyoke chemistry majors, who have been excellent colleagues and friends.

Contents

List of Figures

List of Tables

Chapter 1

An Introduction to Fuel Cells, Perovskite Oxides, and Proton Conduction Therein

1.1 Beyond Fossil Fuel Combustion

As the effects of global climate change become more apparent, reducing atmospheric levels of greenhouse gases has arisen as an important goal for policymakers, researchers, and individuals alike. These efforts will necessarily involve reducing atmospheric levels of CO_2. Carbon dioxide produced by combustion of fossil fuels has been estimated to account for 79 percent of warming potential-weighted emissions in the United States between 1990 and 2010. Increasing CO_2 emissions from electricity generation and transportation activities have driven a 1.7 percent average annual growth rate in U.S. emissions between 1990 and 2007.[1]

Such trends have sparked fresh interest in fuel cells, which offer a means of producing energy with only a fraction of the CO_2 emissions of hydrocarbon combustion, or frequently without any CO_2 emission. However, the current wave

of research is only the most recent entry in the long history of fuel cells. Sir William Robert Grove constructed the first primitive prototype of a hydrogen-powered fuel cell in the nineteenth century, publishing an account of his work in 1839. Scattered international experimentation with fuel cell designs and materials continued through the twentieth century. The oil crisis of the late 1960s and early 1970s together with Cold War anxieties motivated the first concentrated burst of fuel cell research in the United States. Many of the advances made during this period have played a major role in the current wave of design and inquiry.[2]

1.2 Basic Principles of Fuel Cell Operation and Design

Broadly speaking, a fuel cell is a device intended to convert chemical energy directly into electrical energy. Fuel cells are distinguished from batteries by the fact that energy is released from the reactions of substances in the liquid or gas phase, rather than the solid phase as in batteries. Further, reactants are supplied to fuel cells continuously, and reaction products are released continuously. Fuel cells need not be recharged to ensure continuous operation.[1] A generic fuel cell is illustrated in Figure 1.1.

The cell's fuel, typically gaseous hydrogen or methane, is introduced through the fuel flow channels. In a hydrogen fuel cell, the oxidation reaction at the anode catalyst layer yields protons and electrons:

$$2H_2 \rightarrow 4H^+ + 4e^-. \quad (1)$$

The electrons travel into the anode current collector and then into the circuit. The protons travel through the electrolyte towards the cathode. At the cathode, they combine with oxygen and electrons in the reduction reaction:

$$O_2 + 4H^+ + 4e^- \rightarrow 2H_2O. \quad (2)$$

The ionic species and the final product vary with the fuel used.

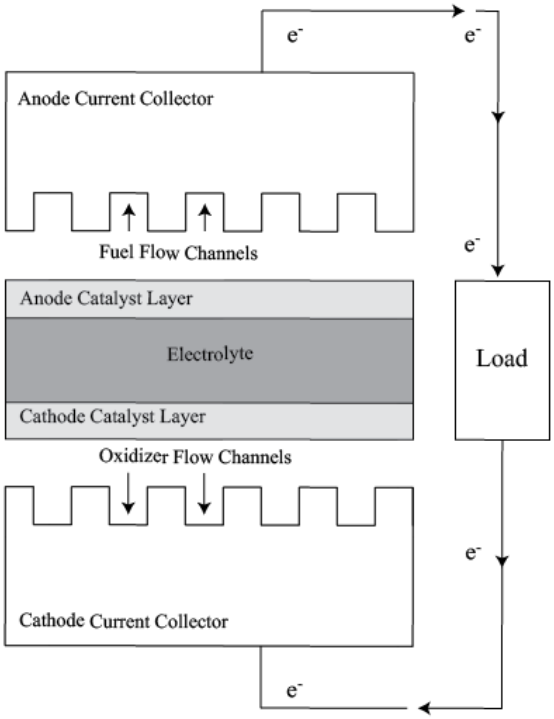

Figure 1.1 A simplified representation of a general fuel cell. Adapted from Mench.[3] The oxidation reaction at the anode produces electrons that travel through the circuit. Meanwhile, ions produced by the oxidation reaction are conducted through the electrolyte, where they combine with electrons and atmospheric oxygen to form a product in the reduction reaction at the cathode.

Wang and coworkers have presented an idealized fuel cell polarization curve. Shown in Figure 1.2, this curve illustrates the fact that losses of potential difference occur at each step in the process described above. At the region of activation polarization (low current densities), the slow kinetics of the reduction reaction at the cathode are primarily responsible for potential losses. As current density increases, ohmic losses due to resistance to ion conduction in the electrolyte—the focus of this work—and resistance to electron conduction in the electrodes dominate. Finally, at high current densities, the rate of the reactant gases' diffusion onto the catalytic layers begins to contribute to the mass transport-related potential drop that occurs when the fuel and oxidant cannot be supplied quickly enough.[4]

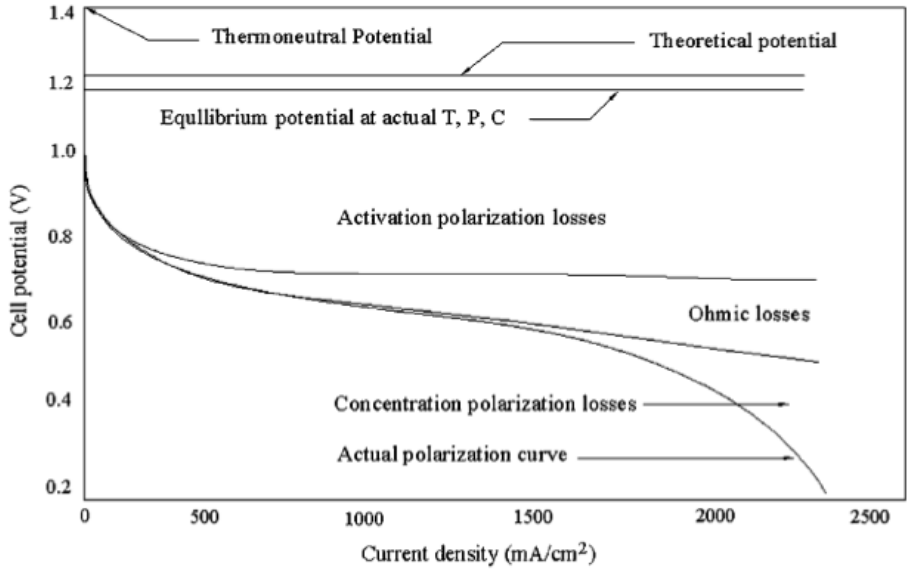

Figure 1.2 An idealized version of a polarization curve for a fuel cell operating under constant conditions.[4] As current density increases, losses associated with different processes in the cell begin to contribute to the drop in potential.

Working voltages below one Volt are common to most fuel cells. To yield higher voltage, multiple cells are connected in series to form stacks. The cathode of one cell in a stack is separated from the anode of the next by a conducting bipolar plate. The necessary voltage dictates the number of cells in the stack. Each section of electrolyte is sealed, end plates are added, and the completed stack is compressed using tie bolts.[1]

1.3 Types of Fuel Cells

Fuel cells are usually classified by their electrolyte material and, where relevant, by their fuel type. This section provides a brief survey of the types of fuel cells that have been the subjects of the most intensive study and development efforts.

1.3.1 Proton Exchange Membrane Fuel Cells and Direct Liquid Fuel Cells

Proton exchange membrane fuel cells (PEMFCs) and direct liquid fuel cells both contain polymer electrolyte membranes, but the former are fueled by humidified hydrogen gas and the latter by one of a number of liquids, including methanol, ethanol, formic acid, and inorganic fuels. The polymer membrane is composed of monomers containing acid groups. When the membrane comes into contact with water, these acid groups dissociate, and the hydrogen-bonded networks that form

can conduct protons generated in the anode reaction. The most commonly used polymer, Nafion®, consists of perflourinated sulfonic acid groups.[2]

Because proton conduction in PEMFCs depends on the presence of liquid water, their optimal operating temperatures range from 80-90 ˚C. Warm-up time is short. Cool operation coupled with high power-to-mass ratios make PEMFCs the natural choice for powering passenger vehicles.[5] However, this low operating temperature also necessitates the use of an excellent and extremely expensive catalyst: platinum[6] or platinum mixed with ruthenium.[2] Platinum catalysts are vulnerable to CO poisoning, which can dramatically reduce efficiency. PEMFC efficiency is also hampered by the occasional movement of reactant and oxidant molecules directly through the relatively permeable electrolyte.[2]

1.3.2 Phosphoric Acid Fuel Cells

In the highly concentrated phosphoric acid (H_3PO_4) solutions employed as electrolytes in phosphoric acid fuel cells (PAFCs), protons produced at the anode jump from one acid molecule to the next, diffusing by the Grotthuss mechanism. While the single phosphoric acid molecule adsorbs well on platinum catalysts, with deleterious effects for electrode efficiency, the phosphoric acid dimmer ($H_4P_2O_7$) that forms at high temperatures (160-220 ˚C) in aqueous solution does not.[2] Higher operating temperatures make catalyst layers less vulnerable to CO poisoning. Waste heat is produced at high enough temperatures to be utilized for thermal energy co-generation, making possible efficiencies approaching 85

percent for cogeneration systems. Standard combustion-based power plants typically run at 33-35 percent efficiency.[5]

However, higher temperatures necessitate longer warm-up and thus slower starting times. PAFCs have lower power-mass ratios than PEMFCs, but they still require expensive, corrosion-resistant Pt-containing catalysts. Because the electrolyte is present in the aqueous phase, small portions are constantly lost to evaporation. Nonetheless, as one of the earliest types fuel cells developed, PAFCs have reached a level of refinement that makes them an appealing option for noiseless, minimally polluting stationary power generation.[3] Approximately 300 PAFC power plants are in operation in Europe, Japan, and the United States.[2]

1.3.3 Alkaline Fuel Cells

In contrast to PAFCs, fuel cells containing less corrosive alkaline electrolytes (usually aqueous solutions of potassium hydroxide) may utilize a range of catalytic materials at the electrodes. While silver and gold prove highly effective, oxides of other metals, nickel, and activated carbon have also been employed.[2] Operating temperature depends on the catalysts used, ranging from 60-250 ˚C. Alkaline cells can operate much more efficiently than cells with acidic electrolytes because of the salutary effects of the alkaline solution on the kinetics of the reduction reaction at the cathode, a major source of potential loss for most fuel cells.

Despite these advantages, alkaline fuel cells have not been widely adopted because of their extreme vulnerability to even small concentrations of CO_2, which reacts with the electrolyte solution to form K_2CO_3.[3] Alkaline fuel cells have been used most successfully to provide power to early spacecrafts, where the purity of the reactant gases could be ensured.

1.3.4 Molten Carbonate Fuel Cells

The electrolyte of a molten carbonate fuel cell (MCFC) consists of a mixture of 62-70 mol percent Li_2CO_3 and 30-38 mol percent K_2CO_3. Maintaining this mixture at the eutectic point—the temperature and composition that represent the coolest possible mixture in which both components are present in the liquid phase—requires working temperatures ranging from 600-650 ˚C. This elevated temperature range confers several advantages, including high tolerance of impurities (thus greater flexibility in fuel sources) and production of high quality waste heat. Moreover, the high rate of hydrogen-carbonate reactions at the electrodes allows use of less efficient catalysts that are far less expensive than platinum.[2] Co-generation MCFC systems can reach efficiencies close to 85 percent.[5]

Kinetic gains in MCFCs are offset by thermodynamic loses, as the efficiency of the overall reaction decreases with increasing temperature.[2] Further, as with PAFCs, small amounts of electrolyte are constantly lost to evaporation and must be replaced regularly. The electrolyte solution often corrodes the

cathode catalysts, causing durability problems.[3] Design is complicated by the fact that CO_2 evolved in the anode reaction must be returned to the cathode to participate in the reduction reaction.[2] Finally, with high operating temperature comes a start-up time slow enough that MCFCs are suitable only for continuous power generation. These difficulties have not prevented the development of several lines of commercially available MCFCs.[3]

1.3.5 Solid Oxide Fuel Cells

Solid oxide fuel cells (SOFCs) contain hard, non-porous ceramic electrolytes. Their operating temperatures are the highest among the common types of fuel cells, ranging from 800-1000 ˚C. Although the extended start-up time required for operation at such temperatures limits their use to continuous stationary power generation, co-generation systems that make use of waste heat could operate at efficiencies higher than 85 percent.[3] As with alkaline and molten carbonate fuel cells, higher operating temperatures make the use of inexpensive, non-noble metal catalysts possible. SOFCs are highly CO-tolerant, allowing the use of lower-grade fuels.[3] A variety of hydrocarbon fuels may be employed. Use of hydrocarbon fuels naturally entails the emission of carbon-containing gases, but SOFCs running on hydrocarbons remain significantly more efficient than hydrocarbon combustion-based energy generation, and their flexibility in fuel sources make them an attractive option for easing the transition to a hydrogen-based energy infrastructure.[3]

The central goal of SOFC research and development efforts involves lowering working temperatures to 500-700 ˚C. This range would preserve the benefits associated with high temperature operation while decreasing thermal stress on components and allowing the use of interconnects made of metal rather than ceramic. Lower operating temperatures would also have the advantage of increasing the safety of SOFC co-generation plants and decreasing operating costs. Achieving lower-temperature operation requires the use of a ceramic electrolyte capable of conducting ions below the standard temperature range.[7]

Thus, exploring the conduction properties of different classes of ceramics represents a promising direction for inquiry. One such class of ceramics consists of the perovskite-structured oxides, or perovskite oxides. This work will detail efforts to determine energetics and patterns of proton conduction in several perovskite oxide systems.

1.4 The Structure of Perovskite Oxides

Perovskite oxides are ceramics with the unit formula ABO_3, where the 12-coordinated A cation is larger than the six-coordinated B cation. Figure 1.3 shows a unit cell of one such material, $BaZrO_3$. While most perovskite oxides are nearly cubic or orthombic,[8] deviations from the ideal structure may be predicted by calculation of the tolerance factor *t*, which is given by

$$t = \frac{r_A + r_B}{\sqrt{2}(r_B + r_O)}, \tag{3}$$

where r_A, r_B, and r_O are the radii of the A, B, and O ions, respectively.

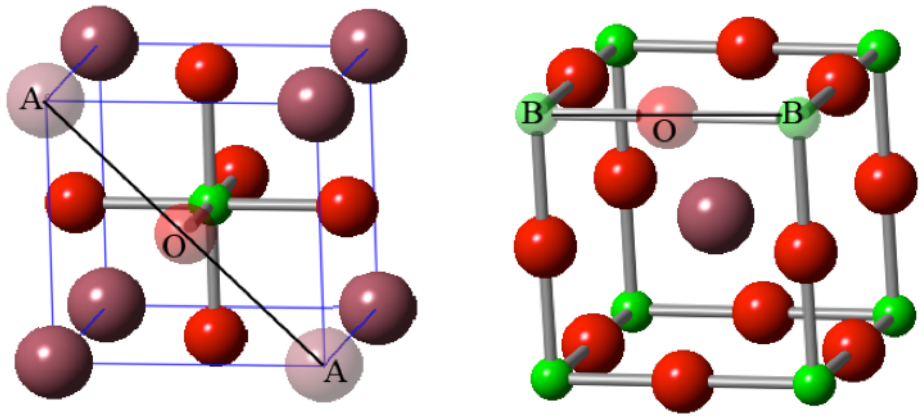

(a) **(b)**

Figure 1.3 (a) and (b) show two equivalent unit cells for $BaZrO_3$, one of the perovskite-structured oxides with the general formula ABO_3. Ba ions (the A ions) are shown in mauve, Zr ions (the B ions) in green, and O ions in red. In (a), the Zr ion is shown at the center of an octahedron made up of O ions, with Ba ions at each corner. The front face shows a diagonal Ba-O-Ba (A-O-A) axis. In (b), the Ba ion is shown at the center. A Zr-O-Zr (B-O-B) axis is shown in black. Replicating either unit cell produces the same lattice structure. Notice that both cells share the same basic grouping of a Ba ion, a Zr ion, and three O ions. This is the true replicable $BaZrO_3$ unit. Additional ions are shown to emphasize the cubic structure.

The tolerance factor compares the lattice size obtained from perfect packing along the A-O-A diagonal with the lattice size obtained from perfect

packing along the B-O-B lines that form the edges of the cube shown in Figure 1.3 (b). If the two lattice constants are equal, $t = 1$, and the structure is expected to be cubic at low temperatures. When $t < 1$, and the lattice size required to accommodate perfect packing on the B-O-B axis is greater, extra space is available along the diagonal. This allows the octahedra formed by O ions surrounding B ions to tilt, distorting the cubic structure.

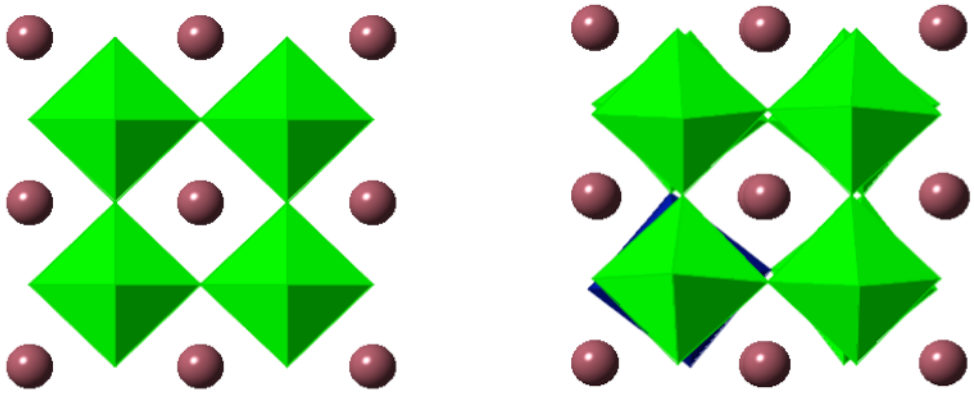

(a) **(b)**

Figure 1.4 A $BaZrO_3$ structure composed of eight unit cells in a 2x2x2 arrangement is shown in (a) for reference. The octahedra formed by zirconia surrounded by six oxygens are shown in green. (b) shows a Y-doped 2x2x2 $BaZrO_3$ unit. The Y-centered octahedron is shown in blue. The octahedra in the doped unit are noticeably tilted. When a larger Y ion replaced a Zr ion, the longer length of the new Y-O-Zr axis increased the spacing along the Ba-O-Ba axis, allowing the octahedra to tilt.

When a fraction of the B ions are replaced with dopant ions, the tolerance factor indicates whether tilting should be expected to increase (when the ionic radius of the dopant is larger than the radius of B) or decrease (when the ionic radius of the dopant is smaller than the radius of B). Tilting effects in one perovskite system are illustrated in Figure 1.4.[9,10]

When two perovskite crystals with the structure described above meet with different orientations, they form a defect known as a grain boundary. Grain boundaries may be grouped into broad categories based on the angle formed by the axis of rotation for each crystal *o* with respect to the normal axes *n* for the crystals. When $o \perp n$, the interface is called a tilt grain boundary, and when $o || n$, the interface is called a twist grain boundary.[11] Both types are shown in Figure 1.5.

Interfaces that do not fall into one of these categories are described as mixed grain boundaries. Additional details about grain boundary structure and properties as well as a discussion of the significant impact of perovskite grain boundaries on proton conduction will be provided in Chapter 2.

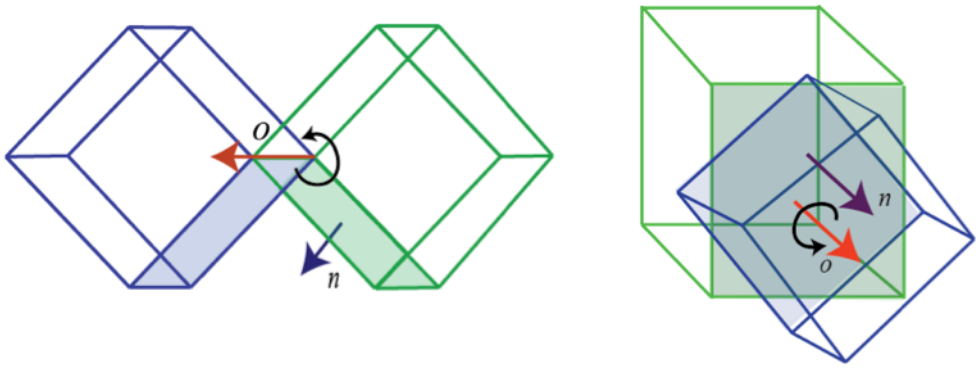

(a) **(b)**

Figure 1.5 A tilt grain boundary between two generic crystals or grains is shown in (a). The axis of rotation *o* is perpendicular to the normals *n* of both shaded crystal surfaces. In (b), a twist grain boundary is shown. The normals *n* for the shaded crystal surfaces lie parallel to the axis of rotation *o*. In a mixed grain boundary, *n* and *o* would describe an angle between 0˚ and 90˚.

1.5 Proton Conduction in Perovskite Oxides

Many perovskite oxides display electrical, ionic, or mixed electrical and ionic conductivity.[12] Among the ion conductors are $BaZrO_3$ and $SrZrO_3$, the proton conductors that are the subjects of this work. Other perovskite-structured proton conductors include $SrCeO_3$, $CaZrO_3$, and $BaCeO_3$. Rates of incorporation for protonic defects are increased by the replacement of a fraction of the +4 ions with lower valence (usually +3) ions. A sample equation[7] for the doping of $BaCeO_3$ with an M^{3+} cation summarizes the doping process for most proton-conducting perovskite oxides:

$$Ce_{Ce}^{x} + M_2O_3 + O_O^{x} \rightarrow 2M_{Ce}^{'} + V_O^{\bullet\bullet} + 2CeO_2. \quad (4)$$

The superscript of each species gives its charge with respect to the ion site it occupies, which is given in the subscript. Species such as Ce that occupy their own sites are uncharged relative to the original occupancy, a state denoted by the x superscript. Each superscripted dot denotes a positive charge, and each prime indicates a negative charge. *V* indicates a vacancy. The introduction of the dopant metal's oxide leads to the replacement of a fraction of the original B cations with the M cation, the creation of an oxygen vacancy, and the formation of an ionic product that leaves the lattice.

The presence of oxygen vacancies allows water molecules present in the gas phase to be absorbed at the surface of the perovskite. During this process, the water molecule dissociates into a hydroxide ion and a proton. The proton forms a covalent bond with a lattice oxygen, and the hydroxide ion fills an oxygen vacancy. This process is given by[7]

$$H_2O_{(g)} + V_O^{\bullet\bullet} + O_O^{x} \rightarrow 2OH_O^{\bullet}. \quad (5)$$

Incorporation of protons from water is exothermic in doped and undoped cerates (such as $BaCeO_3$) and zirconates (such as $BaZrO_3$), a fact consistent with observations that proton incorporation decreases with increasing temperature.[7]

It is convenient to describe a proton that has been incorporated into the lattice and covalently bonded to an oxygen ion as occupying one of four binding sites on the oxygen. The four sites lie in a plane perpendicular to the axis formed by the oxygen and the two adjacent B cations. When every binding site is

occupied, the covalent bonds form right angles with each other, each pointing toward an oxygen atom in an adjacent octahedron.

Density Functional Theory (DFT) studies[9,10,13] suggest that a proton diffusing through the lattice that is bound at any given site may rotate to an adjacent site on the same oxygen (in a rotation step R), move into a site in the same plane on an oxygen in one of the two octahedra its current oxygen is part of (in an intraoctahedral transfer step T), or move into a site on the oxygen in a different octahedron toward which it "points" (in an interoctahedral step I). Each move is illustrated in Figure 1.6.

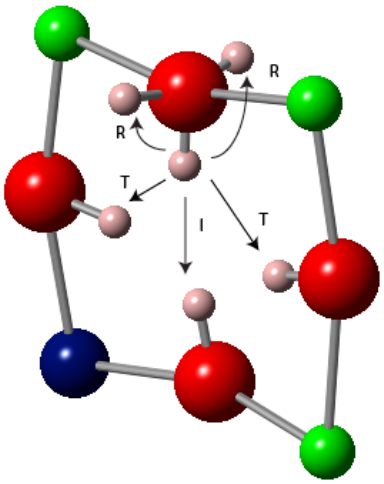

Figure 1.6 A single unit lattice plane. Protons are shown occupying each binding site to which the top center proton might move in a single transition. Notice that two rotations (marked R) and two intraoctahedral transfers (marked T) are possible, as they are from any binding site in the system. Interoctahedral tilting has brought the top and bottom oxygens together, so a fifth transition (an interoctahedral transfer marked I) is possible from the site.

The third move is possible only when octahedral tilting (see Figure 1.4B) has brought the two sites closer together than they would be in a perfectly cubic lattice (4A). Thus, from a given binding site, four or five moves are possible. The average speed of each type of step depends on the type of perovskite and the dopant.[9,10] This process is classified as a Grotthuss-type conduction mechanism, as the proton is passed between adjacent ions that remain relatively stationary.[13]

1.6 Toward a Deeper Understanding of Proton Conduction in Perovskites

This work will describe efforts to generate and understand proton conduction pathways in two different perovskites, $BaZrO_3$ and $SrZrO_3$. Yttrium and aluminum dopants are considered for both perovskites. Chapter 2 will discuss the effects of exchange-correlation functional and pseudopotential choices on minimum energy configurations obtained for stable Y-doped $BaZrO_3$ tilt grain boundary systems. In Chapter 3, the Kinetic Monte Carlo algorithm will be presented as a method for generating long-range conduction pathways in bulk perovskite systems, and past and current efforts to increase the efficiency of the algorithm will be described. Chapter 4 will treat graph theoretical analysis aimed at making sense of the differences in conduction pathways and energetics that mark the four bulk systems considered. This analysis will include a novel application of a centrality measure based on average hitting time.

Chapter 2

Determining the Structural Effects of Yttrium Dopant on $BaZrO_3$ Grain Boundaries

Given the extreme differences between ionic arrangements in bulk systems and in grain boundary systems, it is hardly surprising that the conduction behavior of grain boundaries in ionic solids usually differs significantly from conduction behavior of the bulk material. In many common minerals, ionic diffusion along grain boundaries may be assumed to be several orders of magnitude faster than bulk diffusion. In fact, diffusion through polycrystalline MgO is thought to allow exchange of carbon and transition metals between Earth's mantle and core on a reasonable timescale.[14] The same changes that promote such radical shifts in MgO diffusion could not be expected to leave proton conduction behavior unchanged. Indeed, grain boundary effects on the conduction properties of Y-doped $BaZrO_3$ have been the subject increasing research efforts over the past decade.

2.1 Grain Boundary Effects on Y-doped $BaZrO_3$ Proton Conductivity

Although Y-doped $BaZrO_3$ shows excellent bulk proton conductivity with respect to other perovskite-structured oxide conductors, the overall conductivity of polycrystalline Y/$BaZrO_3$ is significantly lower than optimal bulk conductivity. Experimental values for bulk and grain boundary conduction activation energies are given in Table I. Although values vary based on sample preparation methods, humidity levels, and a host of other factors that make conductivity measurements notoriously difficult to reproduce,[15] the higher barriers to conduction in grain boundaries are apparent.

Table 2.1 Activation energies for proton conduction in bulk and grain boundary sections of Y-doped $BaZrO_3$ with varying dopant levels. While absolute activation barriers vary between studies and dopant percentages, grain boundary activation energies are significantly higher than bulk activation energies.

Y %	Bulk Activation Energy (eV)	Grain Boundary Activation Energy (eV)	Ref.
20	0.45 ± 0.01	0.71 ± 0.02	16
15	0.37	0.74	17
15	0.46 ± 0.01	0.80 ± 0.01	18
10	0.44	0.70	19

High-temperature annealing has been shown to increase grain size and produce more orderly grain boundary and bulk structures, minimizing grain boundary resistance effects. Annealing at 1250 ˚C yielded a 200-fold increase in $BaZrO_3$ conductivity levels with respect to samples annealed at 800 ˚C, and annealing at 1500 ˚C yielded a nearly 500-fold increase with respect to samples annealed at 800 ˚C.[20]

High activation barriers for proton conduction across grain boundaries have been attributed in part to charge density patterns in grain boundary regions. In most ionic solids, the structural differences between grain boundaries and bulk material lower the standard enthalpies for charged defect formation in grain boundary cores. Thus, grain boundary cores may be expected to carry excess positive or negative charge.[21] Experimental[22,23] and theoretical[15] work has shown that $BaZrO_3$ grain boundary cores are positively charged, an effect attributed to segregation of oxygen vacancies to the core.[15] Protons segregation to the grain boundary core has also been shown to contribute to the region's positive charge.[24]

Positively charged grain boundary cores repel positively charged mobile protons, and the increased number of vacancies at oxygen sites decreases the number of proton binding sites available, increasing the O-O distance protons must jump.[15] Higher Y concentrations surrounding grain boundary cores compensate in part for the positive charge. Because Y^{3+} has a larger radius than Zr^{4+} (1.01 Å vs. 0.84 Å), elastic strain promotes the segregation of the dopant into more spacious grain boundary core sites.[23] Negatively charged defects,

particularly electrons, accumulate outside the grain boundary core. This charge gradient forms what is known as the space charge layer, a common feature of doped oxides and other ionic substances. Figure 2.1 illustrates the expected concentrations of protonic and electronic defects in the area surrounding a grain boundary.

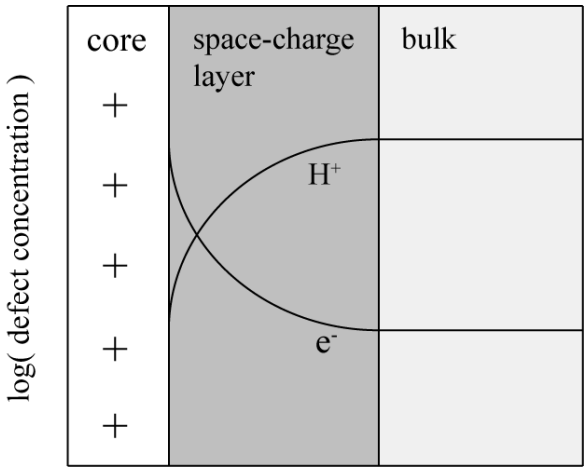

Figure 2.1 A schematic of a grain boundary core and one of the adjacent space charge layers.[22,23] The positively charged grain boundary core repels protonic defects and attracts electronic defects, hindering the passage of protons through the grain boundary. The concentrations of any other positive defects in the lattice also decline near the core.

Although the space charge layer model has gained considerable traction, it has also been posited that grain boundary resistance is the product of the irregular geometries of grain boundaries. These disruptions of the periodic perovskite structure may simply require the proton to move longer distances between

oxygens.[25] Recent work suggests that grain boundary resistance is properly understood as a product of both electrostatic effects and aperiodicity.[26]

2.2 Toward Determination of Proton Conduction Pathways Across a Grain Boundary

While the general tendency of grain boundaries to increase activation barriers for proton conduction has been well documented experimentally, few theoretical studies have considered the migration of a proton across a grain boundary at the atomic scale. Kim and coworkers examined proton conduction in a Σ5 (310) tilt $BaZrO_3$ grain boundary doped with Y at 3.57 percent, the most commonly observed grain boundary in TEM studies of perovskite oxides.[27] The Σ5 (310) grain boundary may be expected to be among the most stable grain boundary structures, as the Σ5 classification refers to the fact that 1/5 of the atomic sites in each grain coincide when the grains are superimposed. If we assume that the lowest energy, most stable arrangement occurs when each ion is in its normal lattice site, it is reasonable that the most stable superimposition of grains would be the one that preserves the highest fraction of these positions.[28]

In order to trace out possible low-energy pathways across the grain boundary, Kim and coworkers determined the most stable Σ5 (310) tilt grain boundary structure. Density functional theory (DFT), a technique that will be described in more detail in the next section, was used to determine the energies of

the geometrically optimized possible structures. Four possible dopant sites labeled A-D (shown in Figure 2.2) were identified at the core of the most stable grain boundary structure. The structure with the dopant at the B site was determined to be most stable, and the energy barriers to each possible proton move between binding sites in the structure were calculated. Using these energies, possible low-activation energy pathways across the grain boundary were identified.[27]

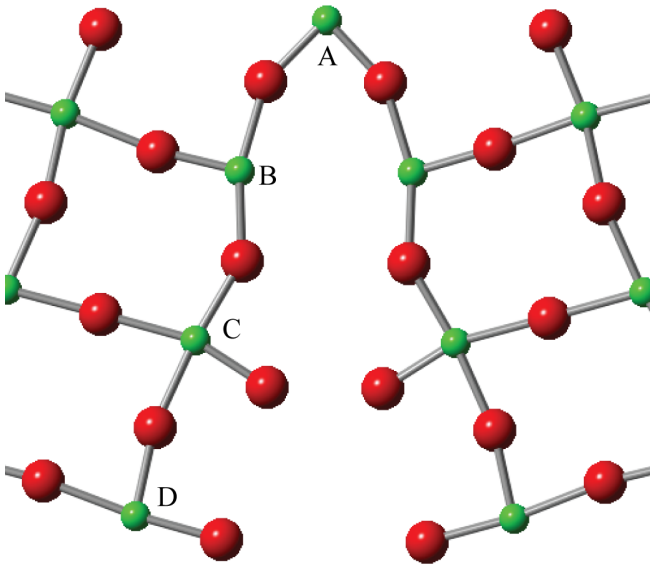

Figure 2.2 A portion of a single lattice plane from Kim's optimized Σ5 (310) tilt grain boundary structure showing the possible sites at which a dopant ion may be substituted for a Zr ion (shown in bright green). Ba ions have been omitted for clarity. Substituting Y for Zr at one of these sites gives a dopant level of 3.57 percent when all of the Zr sites in the system (and not just those shown here) are considered.

Previous studies have employed kinetic Monte Carlo simulations and dynamic programming (see Chapters 3 and 4) to generate all possible periodic long-range conduction pathways through bulk perovskite systems, including Y-doped $BaZrO_3$.[9,10] Probability-weighted averages of the highest activation barriers in each pathway yielded rigorous estimates of activation barriers for proton conduction in the systems of interest. Constructing long-range conduction pathways requires full characterization of the system, including the optimal energies of the structure with a single proton occupying each binding site, the energies of each possible proton transition between binding sites, and the normal mode frequencies for binding site and transition state structures.[9,10] As a first step toward this full characterization, optimal energies for Kim's grain boundary structures with dopant in each of were the four sites were determined using DFT. The results proved an interesting demonstration of the effects of the approximations chosen in the course of DFT calculations.

2.3 Reducing the Complexity of the Many-Body Problem to Determine Ground State Energy

Because the precise ground state energy of any system with interactions more complex than those present in the hydrogen atom cannot be determined analytically, calculating a reasonably accurate ground state energy for a perovskite grain boundary system requires a series of approximations. The problem may is simplified by application of the Born-Oppenheimer

approximation, with assumes that light, quick electrons respond instantaneously to the motion of relatively slow-moving, heavy ionic nuclei. Thus, the motion of the nuclei and the electrons may be treated separately, with electron behavior playing out in the potential generated by a static configuration of nuclei.

Even when ion nuclei are fixed, electron-electron interactions and electron-ion interactions must be accounted for, and electron positions must be optimized based on these interactions. Electron-electron interactions may be treated using density functional theory (DFT). DFT rests on Hohenberg and Kohn's proof that the total energy of an interacting electron gas is a functional of the gas's electron density. Hence, the many-electron problem presented by the gas can be mapped onto a series on non-interacting electrons subject to potentials generated by the other electrons in the system. The set of wave functions that minimizes the total energy functional consists of the self-consistent solutions to the equation

$$\left[\frac{-\hbar}{2m}\nabla^2 + v_{ion}(r) + v_H(r) + v_{XC}(r)\right]\psi_i(r) = \varepsilon_i\psi_i(r) \tag{1}$$

where the Hartree potential v_H is given by

$$v_H(r) = e^2\int\frac{n(r')}{|r-r'|}d^3r'. \tag{2}$$

$n(r)$ refers to the electron density at a point r, equivalent to the probability density for any of N electrons in the system being at the point r:

$$\rho(r) = 2\sum_i^N \psi_i^*(r)\psi_i(r). \tag{3}$$

The $v_{ion}(r)$ term gives the static electron-ion potential, and $v_{XC}(r)$ refers to the exchange-correlation potential, given by

$$v_{XC}(r) = \frac{\delta E_{XC}[n(r)]}{\delta n(r)}. \quad (4)$$

$E_{XC}[n(r)]$ is the exchange-correlation functional. The exchange-correlation energy is the sum of the exchange energy (reduction in energy due to the wave function's antisymmetry) and the correlation energy (the difference between the true many-bodied energy of the system and the energy approximated by the Hartree-Fock method). Exchange energy is itself a function of the electron density function. Once an approximation for $E_{XC}[n(r)]$ is given, determining the total energy is a matter of solving the eigenvalue problem posed by Equation 1.

Employing periodic boundary conditions would seem to complicate the problem by introducing an infinite number of electrons and fixed nuclei whose interactions must be accounted for. However, according to Bloch's theorem, each electronic wave function can be given as the sum of a basis set of plane waves. Depending on the boundary conditions of the system, a set of *k* points may be constructed where electronic states are represented, and extremely accurate approximations may be produced by the calculation of only a few *k* points' wave functions. Because plane waves with lower kinetic energy are weighted more heavily in the wave functions, the basis set is truncated at a chosen energy cutoff.

In the areas close to the ionic nucleii, where wave functions oscillate quickly, the plane wave basis set cannot adequately expand the electronic wave functions. The behavior of valence electrons rather than core electrons tends to

dictate the properties of crystals, though, so core electrons may effectively be removed and replaced with weak pseudopotentials acting on pseudo wave functions. When an appropriate pseudopotential is used, the effects outside the core region are indistinguishable from the effects produced by the core electrons. The construction of a pseudopotential begins with the selection of an exchange-correlation functional. An initial pseudopotential expression with variable parameters is generated. The parameters are optimized until the pseudo-ion system displays the same eigenvalues as the electronic system is will replace, and the pseudo wave functions are equal to the electronic wave functions beyond a certain cutoff radius. When an appropriate pseudopotential is in place, simplifying the treatment of electron-ion interactions, the many-body problem has been reduced to manageable proportions.[29]

2.4 Exchange-Correlation Functionals

Many exchange-correlation functional approximations have been developed for use in different systems, but only three general approaches that have been applied in this work will be described here. The first is the local-density approximation, or LDA. In the LDA, it is assumed that the exchange-correlation energy for each electron at some point *r* in the electron gas is equivalent to the exchange-correlation energy that would be obtained if the gas had the same density throughout that it displays at point *r*.[29] The approximation has the general form

$$E_{XC}^{LDA}[n_{\uparrow},n_{\downarrow}] = \int d^3 r n(r)\varepsilon_{XC}[n_{\uparrow}(r),n_{\downarrow}(r)], \quad (6)$$

with $\varepsilon_{XC}(n_\uparrow, n_\downarrow)$ giving the exchange-correlation energy per particle in the gas.[30] Despite the fact that this approximation ignores the effects of nearby variation in electron density, it often yields excellent results.[29]

The LDA is recognized as sufficiently accurate for calculating ground state energies for a number of applications, but for some applications it is desirable to consider the variation in the density of the electron gas, which is accomplished by incorporating the gradient of the electron density at different points to form a generalized gradient approximation (GGA). These approximations take the general form

$$E_{XC}^{LDA}[n_\uparrow, n_\downarrow] = \int d^3 r f(n_\uparrow(r), n_\downarrow(r), \nabla n_\uparrow, \nabla n_\downarrow). \quad (7)$$

One commonly employed GGA is the PW91 approximation.[17] Another potential in common use is the PBE functional, which attempts to provide a simpler alternative to the complex, highly parameterized GGA functional while maintaining the most accurate features of the LDA and introducing only the energetically significant gradient corrections.[31]

2.5 Energetic and Geometric Optimization Using VASP

The Vienna *Ab-Initio* Simulation Package (VASP)[32] employs exchange-correlation functionals, pseudopotentials, and periodic boundary condition approximations to calculate approximate ground state energies for ionic systems. Electronic ground states are calculated self-

consistently for each configuration of nuclei. This process involves setting up the Hamiltonian with trial wave functions and charge densities, and then optimizing these functions until they closely approximate the true functions.[32]

Multiple algorithms for optimizing the positions of the nuclei exist, but calculations described in this work have employed only the conjugate gradient (CG) method. Nuclei positions are optimized with respect to the potential energy surface generated by the electrons in the system. From the point on the potential energy surface corresponding to the initial configuration, nuclei are moved in the direction of steepest descent, in the direction opposite the gradient at the initial point. When a local minimum along the line is reached, a new direction is selected. This direction is a linear combination of the previous direction vector and the gradient at the current point, and it is conjugate to the previous direction. Each time a conjugate direction is selected, the dimension of the area to be explored is reduced by one. Eventually, the space becomes zero-dimensional, and the configuration at this point represents the minimum energy.[29] The geometric optimization of the system is said to have converged when the difference between two successive configurations drops below a specified cutoff value.[30]

2.6 Optimal Grain Boundary Structures and Energies

Preliminary optimizations indicated that grain boundary structures with dopant in the A site or the B site were more stable than structures with dopant at the C or D sites. Thus, these two structures were optimized using each of the three exchange-

correlation functionals discussed above: LDA, PW91, and PBE. For each optimization, a 2x2x2 Monkhorst set of *k* points were constructed, and an energy cutoff of 500 eV was used to limit the plane-wave basis set. The dimensions and volume of the simulation box were relaxed. The optimal energies for each structure using each functional are reported in Table II. The results from each functional will be discussed in more detail in the following sections.

Table 2.2 The energies of optimized grain boundary structures with dopant at the A or B site. All energies and relative energies are reported in eV. Notice that two of the three functionals yielded lower optimal energies for the structure doped at the B site.

Functional	LDA		PW91		PBE	
Result Type	Energy	Relative Energy	Energy	Relative Energy	Energy	Relative Energy
Site A	-1237.2	0.2	-1138.5	0.9	-1133.4	0.0
Site B	-1237.4	0.0	-1139.5	0.0	-1133.3	0.1

2.6.1 Results from the LDA Functional

The optimized structures grain boundaries in with the dopant in the A and B sites are shown in Figures 3 and 4, respectively.

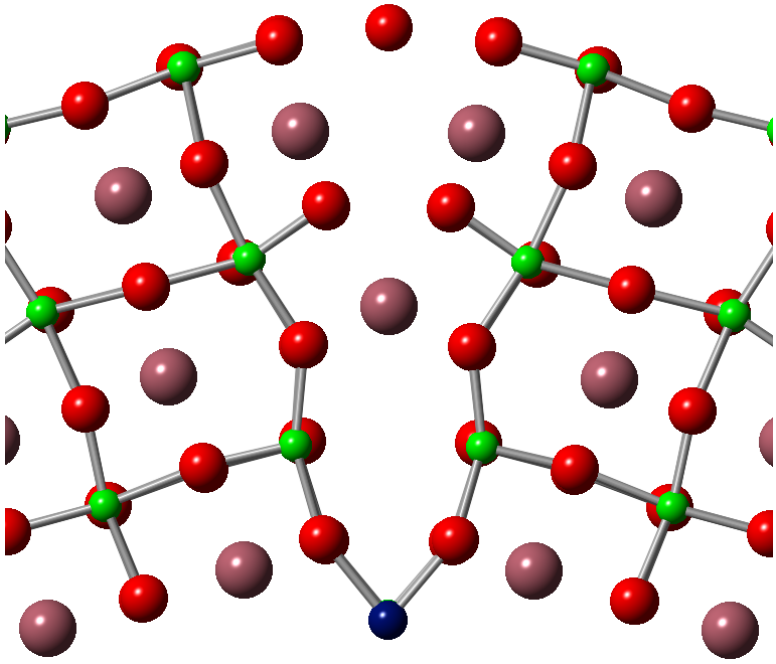

Figure 2.3 Kim's grain boundary structure with the dopant (dark blue) in the A site. This structure was optimized using the LDA functional. Some ions have been omitted for clarity, and periodic images of ions are not shown. This structure maintained its symmetry about the central vertical axis.

While the structure doped at the A site remained largely symmetrical about a vertical axis, the structure doped at the B site displayed significant asymmetric distortions. The latter was determined to be approximately 0.23 eV lower in energy than the former.

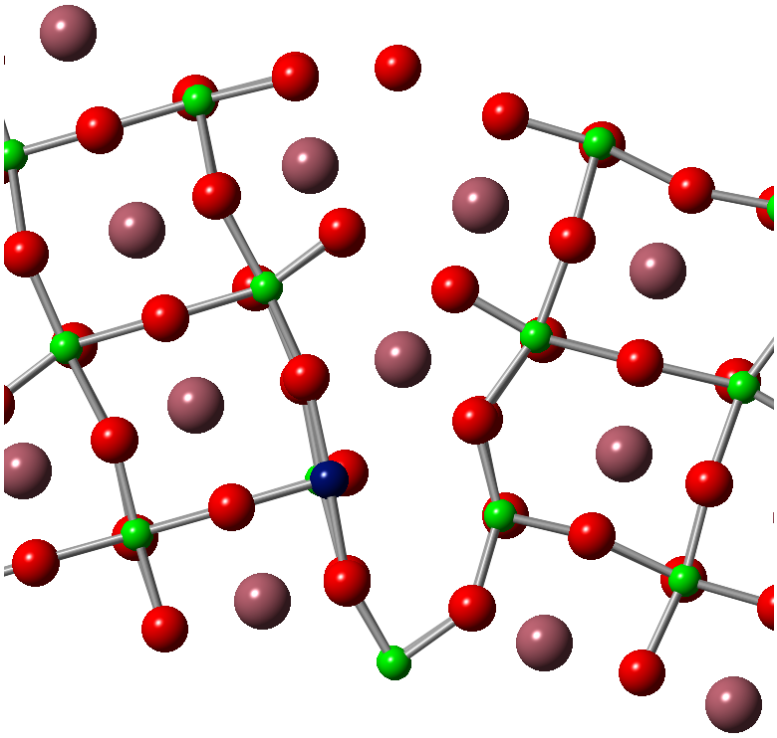

Figure 2.4 Kim's grain boundary structure doped at the B site and optimized using the LDA functional. Notice that the extreme asymmetric distortions introduced as a result of the asymmetric doping.

2.6.2 Results from the PW91 Functional

The grain boundary structures doped at the A and B sites and optimized using the PW91 functional are shown in Figures 5 and 6, respectively. The structure doped at the B site was determined to be the lower in energy by 0.99 eV. In general, the structures show the same patterns as the structures optimized using the LDA functional. The grain boundary doped at the A site remained symmetrical upon optimization, while the grain boundary doped at the B site was asymmetrically distorted. These distortions appear more extreme than the distortions produced in the same structure during optimization using the LDA functional, and they may

account for the larger energy gap between the two structures yielded by optimization using the PW91 functional.

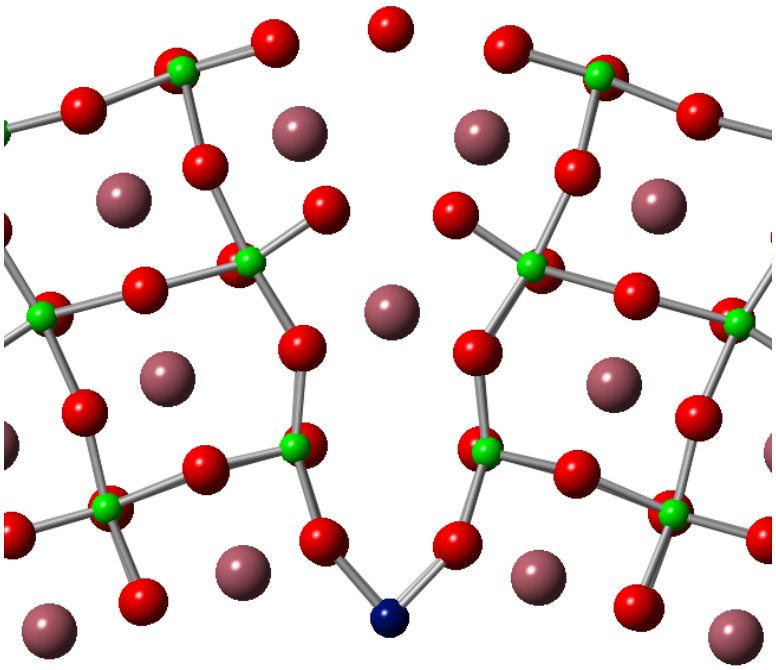

Figure 2.5 The grain boundary doped at the A site and optimized using the PW91 functional. The grain boundary remained almost perfectly symmetric about the vertical axis, and the structure is extremely similar to the same structure optimized using the LDA functional.

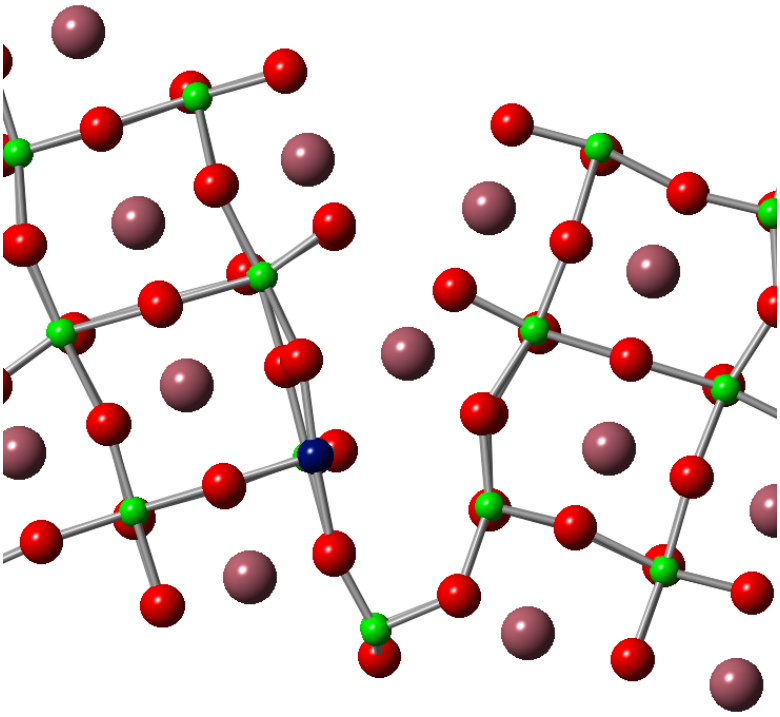

Figure 2.6 The optimized structure for the grain boundary doped at the B site. Optimization was performed using the PW91 functional. Notice that the asymmetric distortions on the left side of the structure, particularly in the unit cell above the dopant, are more extreme than the distortions generated by optimization using the LDA functional.

2.6.3 Results from the PBE Functional

Optimizations performed using the PBE functional yielded energy values suggesting that the structure doped at the A site is more stable by 0.13 eV than the structure doped at the B site. The optimized structure doped at the A site is shown in Figure 2.7. Of the three functionals used, only the PBE functional produced asymmetric distortions in the structure doped at the A site.

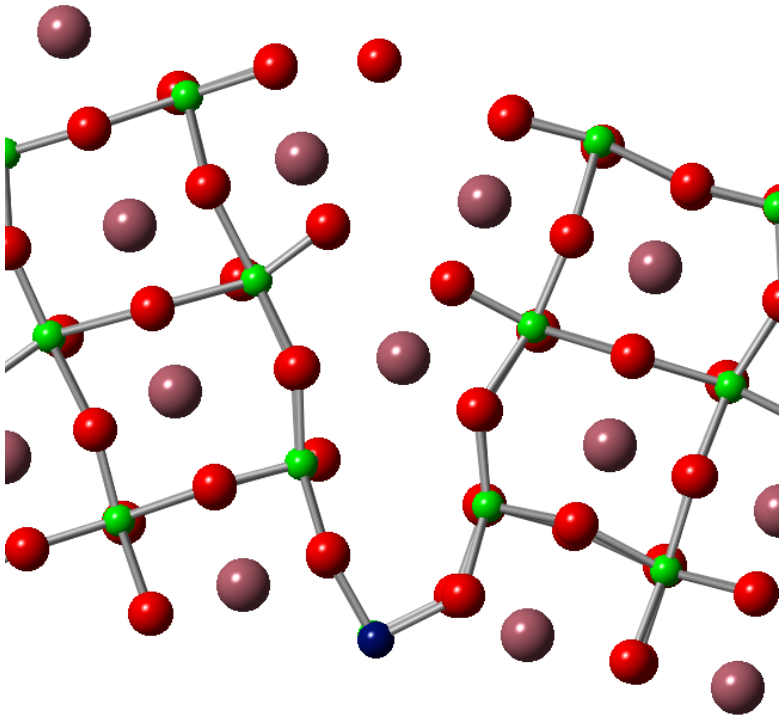

Figure 2.7 The grain boundary structure doped at the A site and optimized using the PBE functional. The resulting distortions are less extreme than the distortions in structures doped at the B site, but they are not entirely dissimilar to those present in the structure doped at the B site and optimized using the LDA functional.

Although the structure doped at the B site is significantly more distorted than the structure doped at the A site, the fact that both show asymmetric distortions might account for the relatively small energy gap between them.

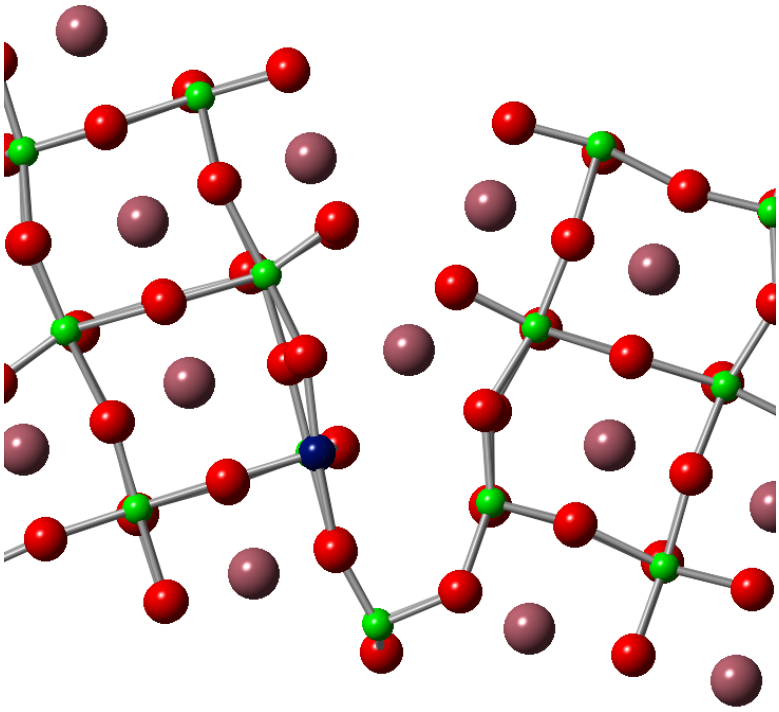

Figure 2.8 The grain boundary structure doped at the B site and optimized using the PBE functional. It is interesting to note that the distortions in this structure are almost identical to the distortions in the same structure optimized using the PW91 functional.

2.7 Conclusions

The variation in optimized structures and relative energies demonstrates the significant effects of the chosen functional on optimization results. Determining which functional has performed best is not a simple matter, and none of the individual results can be considered complete without reference to the functional used to generate them. The most recent theoretical studies of Y/$BaZrO_3$ grain

boundary structure have employed the PBE functional, so use of this functional would yield results more comparable to similar work.[24,27]

A few general trends may still be observed. In each case, asymmetrically-doped optimized structures were more distorted than structures doped at the A site. Further, the lowest energy structure for each functional underwent at least minor distortions. It is not entirely apparent, though, that the shifts in simulation box shape and volume that allowed the most extreme distortions to occur realistically reflect the behavior of a physical grain boundary. In an experimental system, forming grain boundaries would be surrounded by large sections of bulk material, so it is not clear whether such broad distortions could occur. Further review of similar studies might shed light on the simulation box relaxation issue.

Chapter 3

Kinetic Monte Carlo Simulations to Determine Probable Conduction Pathways in Perovskite Systems

While graph theoretical methods have proved extremely useful in determining probable conduction pathways and the general characteristics of probable pathways in perovskite systems (see Section 4.2), kinetic Monte Carlo (KMC) simulations offer an alternate, complementary approach for determining pathways by predicting the movement of a proton through the system. In this section, the advantages of KMC simulations over molecular dynamics simulations will be discussed and a general algorithm will be presented, along with the process for applying this algorithm to simulate proton conduction. A novel variation on this general algorithm will be described, and its results and utility in determining proton conduction pathways will be assessed.

3.1 KMC Algorithms as Solutions to the Time Scale Problem

Beginning in the 1990s, as available computing power increased, molecular dynamics (MD) simulation emerged as the first-principles method of choice for

modeling the evolution of systems over time on the molecular level.[33] MD simulations model system changes by propagating the classical equations of motion ahead in time and moving atoms along the resulting trajectories. When the potential used to calculate atomic forces in the system describes the system well, MD simulations can yield very accurate information about the behavior of the system.[34] Although these features make MD simulation a powerful modeling tool, time scale issues can limit its application. In order to resolve atomic vibrations, the time steps used in MD integration must be very short—on the order of 10^{-15}, limiting simulation times to less than a microsecond.[34] System behavior typically unfolds along multiple time scales, though, and studies of structure, transport, and other key properties often need to simulate longer time spans than are possible using MD.[33,34]

Kinetic Monte Carlo (KMC) simulations provide a stochastic method for simulating behavior over extended time scales.[33,34] KMC simulations may be performed in systems whose evolution over time is marked by a series of relatively infrequent transitions between states separated by minor vibrational activity. KMC methods yield trajectories consisting of many such state-to-state transitions. Intervening vibrations are neglected.[34] KMC algorithms can be thought of as providing solutions to the master equation

$$\frac{\partial P(\sigma,t)}{\partial t} = \sum_{\sigma'} W(\sigma' \rightarrow \sigma) P(\sigma',t) - \sum_{\sigma'} W(\sigma \rightarrow \sigma') P(\sigma,t), \qquad (1)$$

where σ and σ′ represent successive states of the system, $P(\sigma,t)$ is the probability that at time t the system is in state σ, and $W(\sigma' \rightarrow \sigma)$ represents the probability per unit time that the system will transition from σ′ to σ.[35]

In many solid-state systems, including the perovskite systems discussed here, the states σ and σ′ correspond to the system's occupation of two different energy wells. Moving from one state to the next requires the system to overcome the energy barrier that separates the two wells. The time separating transitions is long enough to allow the system to "forget" what process brought it to its current state, so the probability of each transition that represents an escape route from the currently occupied energy well i to some adjacent well j depends only on the characteristics of i, j, and the ridge connecting them. No matter which well the system occupied before well i, the probability per unit time that the system will transition from i to j can be given by a single rate constant k_{ij}.[34] Hence, transitions can be treated as random, independent events, allowing us to model the evolution of the system as a Poisson process, a treatment that is consistent with the master equation (Equation 1).[35] This "infrequent event" model is highly general and has been used to model a wide range of processes. Early applications include simulations of crystal growth, surface diffusion, and reaction kinetics.[33]

3.2 A General Kinetic Monte Carlo Algorithm

This section describes what is perhaps the most commonly employed KMC algorithm, which was proposed by Bortz, Kalos, and Lebowitz in 1975 as a method of simulating Ising spin systems. It is commonly known as the BKL algorithm or continuous time KMC.[34] The simulation begins with the system occupying some initial state *i*. Rate constants k_{ij} have already been calculated for every possible move from state *i* to some other state *j.* These rate constants are treated as objects with lengths corresponding to their values, and they are strung end to end to form a larger object corresponding to the sum of the rate constants for every possible move from state *i,* $k_{tot.}$ A random number *r* between zero and one is generated, and this number is multiplied by the length of k_{tot} to choose a random position along the k_{tot} object, which will correspond to the rate constant object for one of the possible moves.

Thus, moves are selected in proportion with their probability of occurring in the physical system. The move described by the chosen rate constant is then executed, moving the system into one of the states adjacent to *i.* Figure 3.1 illustrates this selection process. Every move selected in this manner is executed. This feature distinguishes the BKL algorithm from "null event" algorithms in which a selected move might be rejected to ensure that moves occur at rates proportional to their probabilities.

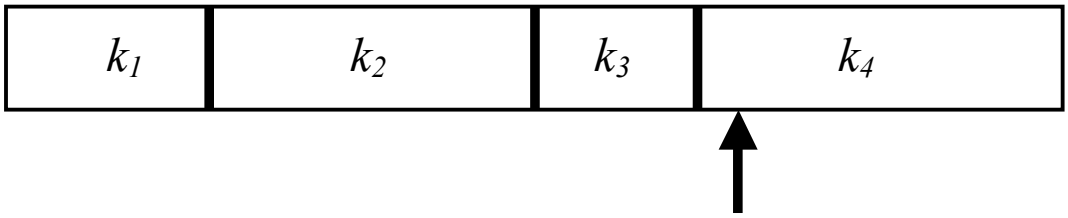

Figure 3.1 The k_{tot} "object" used to select a move from one state to an adjacent state. In this illustration, the position rk_{tot} lies along the k_4 object, so of four possible moves, the one described by k_4 will be selected.

After the chosen move has been executed, the simulation's clock is advanced by a random time drawn from an exponential distribution determined by the value of k_{tot}:

$$t_{draw} = -\frac{1}{k_{tot}}\ln(r) \tag{2}$$

where r is again a random number between zero and one. At this point the move selection procedure begins again.[34]

3.3 Generating Proton Conduction Pathways Using Kinetic Monte Carlo Simulations

The infrequent event model that forms the basis for KMC simulations corresponds well with the long-term conduction behavior of perovskite systems. Each state or energy well represents an optimized configuration with a single proton occupying one of the binding sites in the system. Before the simulation

begins, rate constants for every possible transition are calculated using barriers to transition and frequencies yielded by density functional theory (DFT) calculations. Moves between states are selected randomly using the rejection-free procedure described above.

After each move, the binding site occupied by the proton in the new state is recorded. The resulting list of binding sites represents the trajectory of the proton throughout the simulation. Following the simulation, another program is used to extract conduction pathways of different lengths from the trajectory and sort these paths by probability. Each possible move from a state with the proton occupying some binding site *i* to another state with the proton occupying some site *j* is assigned a weight w_{ij}, which is given by

$$w_{ij} = -\ln(p_{ij}) = -\ln\left(\frac{k_{ij}}{\sum_j k_{ij}}\right), \tag{3}$$

where p_{ij} is the probability of transition from state *i* to state *j*, which is equal to the rate constant for the transition, k_{ij}, normalized by the sum of the rate constants for all possible transitions away from state *i*. The total weight for a path is equal to the sum of the weights of each step involved, so the highest-probability paths of a given length are those with the lowest weights. One such pathway, the most probable for the Al-doped $SrZrO_3$ system, is shown below in Figure 3.2. Conduction pathways for perovskite systems produced using KMC simulations have been shown to be in good agreement with pathways generated using a graph theoretical approach.[9,10]

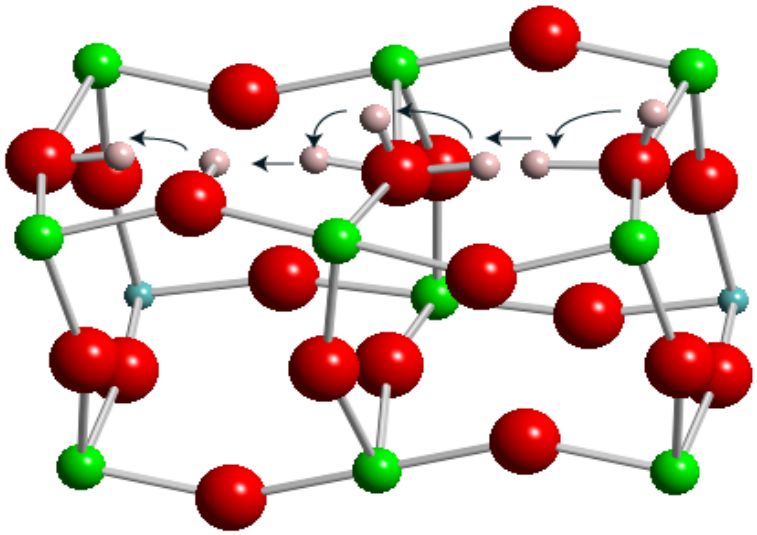

Figure 3.2 The most probable seven-step conduction pathway in the Al-doped $SrZrO_3$ system (RIRRTTR). The final step leading back to the periodic image of the first binding site is not shown. Protons have been placed in each location the single moving proton occupies as it traverses the path—each site that would be recorded in the proton's trajectory.

3.4 Attempts to Increase Kinetic Monte Carlo Simulation Efficiency

Although the standard KMC algorithm as described in Section 3.2 yields simulation on much longer time scales than would be feasible using MD methods, lengthy KMC simulations can still prove computationally expensive. This section will present a sampling of problems that often slow KMC simulations, describe paradigmatic algorithms that have been developed to circumvent these issues, and discuss their potential effectiveness for simulations of proton conduction behavior in perovskite systems.

3.4.1 Efficient Search Algorithms

One of the most time-intensive steps of many KMC algorithms involves picking out the event based on the random number chosen. The method that corresponds most closely with the intuitive notion of pointing to a section of the k_{tot} object introduced in 3.2 requires the creation of an array of partial sums of the rate constants for possible moves. A linear search of the array is performed, and the index of the first element greater than or equal to rk_{tot} indicates the rate constant chosen.[34] Computation time required for a single move choice increase linearly with the number of possible moves.[33]

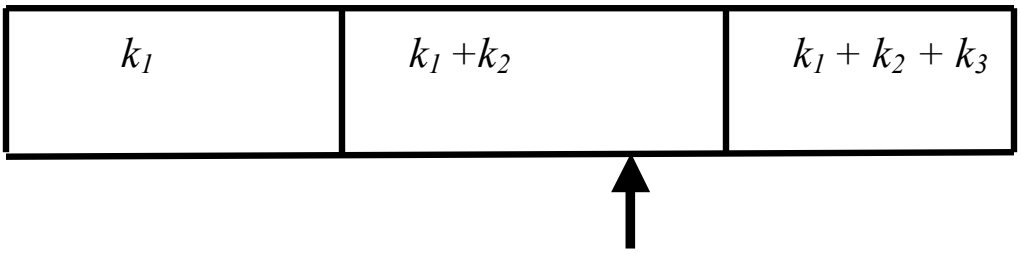

Figure 3.3 An illustration of the simplest algorithm for choosing a KMC move. In this example, $rk_{tot} \leq k_1 + k_2$, so the move corresponding to k_2 will be selected.

When a large number of moves are possible from a given state, this linear search method becomes burdensome. In a crystal growth simulation, for example, a move may be constituted by the occurrence of one of several processes (adsorption, desorption, diffustion, etc.) at any of the hundreds or thousands of sites forming the crystal lattice. Hence, it is often desirable to implement a more

efficient search method, many of which have been developed to facilitate database searches in other fields. This section describes two frequently employed methods.[33]

3.4.1.1 *n*-level Linear Search Methods

In the simplest case where $n = 2$, this method requires the construction of a 2D square matrix with elements consisting of the rate constants for each process. The sum of the elements in each column, $k_{c,tot}$, is computed. The first column C such that

$$\sum_{c=1}^{C} \frac{k_{c,tot}}{k_{tot}} \geq r \tag{4}$$

is chosen. Next, the move corresponding to the first element of the column, k_i, for which

$$\left(\sum_{c=1}^{C-1} k_{c,tot} + \sum_{i=1}^{i} k_i \right) \geq r k_{tot} \tag{5}$$

is chosen. The computational savings depend on the number of possible moves and the number of levels used. For example, if 10^6 moves are possible, a two-level search will be approximately 10^3 times faster than a linear search.[33]

3.4.1.2 Binary Search

Binary search-based move selection methods offer additional high-efficiency alternatives to linear search. Effectively implementing these methods requires the

construction of a data structure known as a binary tree. A binary tree consists of a series of nodes, with a single node at the first level and at each subsequent level two nodes linked to each node in the level above. In a balanced binary tree, nodes at the lowest level contain the rate constants for each possible move, and nodes at higher levels contain the sums of their two daughter nodes. Alternately, in an unbalanced binary tree, one node at each level below the first level contains a rate constant corresponding to a possible move. The other node contains the sum of the nodes below it. These data structures are illustrated below in Figure 3.4.

At the start of the search process, rk_{tot} is the search value. If the search value is less than the left branch, the left branch is selected, and the search value remains the same. If the search value is greater than the left branch value, the right branch is selected, and the left branch value is subtracted from the search value. The process continues until a rate constant is reached and the corresponding move selected. A balanced or unbalanced tree may be used. Computational time is proportional to $\log_2$ of the number of possible moves, so a binary search of 10^6 rate constants is 10^4-10^5 times faster than a linear search of the same rate constants.[33]

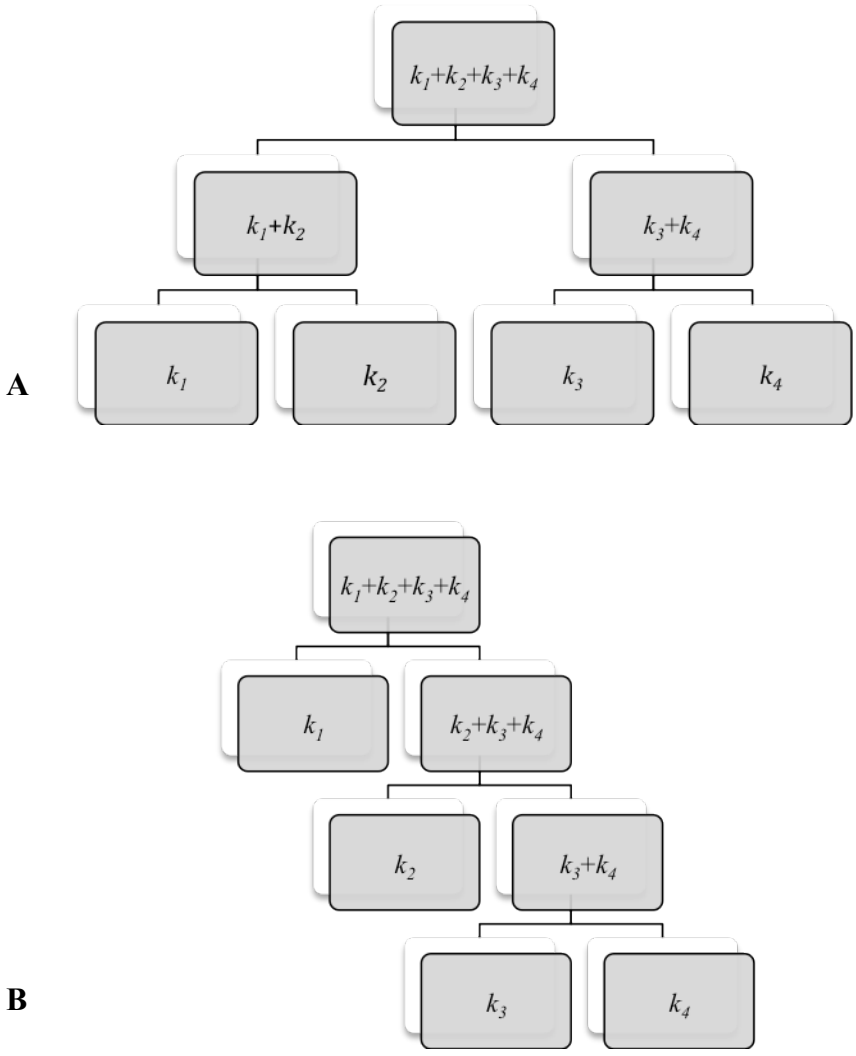

Figure 3.4 A shows a balanced tree diagram that may be employed for selecting a KMC move, and B shows an unbalanced tree diagram for the same purpose. They may be used equivalently in the move selection process.

Hence, the computational savings realized by implementing either an *n*-level or binary search depends entirely upon the number of elements that must be searched at each iteration of the algorithm. From any binding site in a perovskite system, only four or five transitions are possible. Performing a linear search of an

array containing four or five rate constants is not sufficiently costly to warrant use of a more complex search method.

3.4.2 Temporal Coarse-Graining with the τ-Leap Method

The KMC algorithm described so far yields highly detailed information about the behavior of the system: a log each transition the system undergoes and the time of each transition. Suggesting that such detailed information may not be required to yield an adequate simulation of system behavior, Gillespie described a method of temporal coarse-graining known as τ-leaping, which is applicable to systems whose transitions may be described as occurrences of chemical reactions. For certain systems, an adequate simulation might be one that records which reactions have occurred over a subinterval spanning what would otherwise have been two or more time steps.

The τ-leap method is designed to provide information about the behavior of a system at a more general level. Its central function is $Q(k_1,...,k_M \mid \tau;x,t)$, the probability that given a certain configuration x, reaction channel R_j will fire precisely k_j times during the interval $[t,\ t+\tau)$ for $j=1,...,M$. Obtaining a value for Q for an arbitrary τ is prohibitively difficult, but Q may be approximated if τ is restricted to values small enough that any state change over the interval $[t,\ t+\tau]$ will have only a trivial impact on the propensity functions a_j of each reaction channel (the probability that for some configuration a reaction channel will fire

within the system in the next infinitesimal time interval). This constitutes the leap condition. In this case, k_j, the number of firings of a reaction channel R_j, constitutes a Poisson random variable:

$$k_j(\tau;x,t) = P(a_j(x),\tau) \tag{7}$$

for $j=1,...,M$. As each of $k_1,\ldots k_M$ are statistically independent, Q can be given by

$$Q(k_1,...,k_M \mid \tau;x,t) = \prod_{j=1}^{M} \rho_P(k_j;a_j(x),\tau). \tag{8}$$

$P(a,\tau)$ may be generated by numerical means, so at each iteration of the algorithm a sample value k_j representing the number of times R_j fires during the interval $[t, t + \tau)$ is produced. With each firing of R_j, the composition of the system changes by v_j molecules. Thus, the net state change λ may be calculated:

$$\lambda = \sum_{j=1}^{M} k_j v_j . \tag{9}$$

Once λ has been calculated for the sample values of each k_j as well as $a_j(x)$ and τ, the leap is made by advancing the clock from t to $t + \tau$ and updating the positions from x to $x + \lambda$.[6]

Although the τ-leap method has been shown to perform as well as more finely-grained simulations in common systems—a growing crystal, for example—while saving computational resources, it would not be suitable for conduction pathway determination. Any state change that shifts a perovskite system from a state with the proton located in one binding site to a state with the proton located in a different binding site has a major impact on the propensity functions of each

potential proton transition, as a unique set of four to five proton transitions is possible from each site. Changing binding sites changes the set of possible transitions in a non-trivial fashion, so the leap condition could never be met. While Gillespie aimed at eliminating the timed record of each move made by the system, it is precisely this detailed, ordered record which allows the use of KMC simulations to determine conduction pathways.[36]

3.4.3 Executing Multiple Moves at Each Time Step with Multiscale Kinetic Monte Carlo (MSKMC) Simulations

DeVita, Sander, and Smereka have developed an efficient algorithm for KMC simulations of epitaxial surface growth to accommodate the varying time scales of events in surface systems. In their systems of interest, five types of transitions consisting of atom hops are possible: hops taken by adatoms with no in-plane bonds as well as hops taken by atoms with between one and four bonds. The rate for each type of transition is given by

$$w_n = \exp(-nk_BT), \tag{10}$$

where n is the number of bonds.

Rates for each type of transition are drastically different. In a Cu system at 600 K, for example, 148 adatom hops occur for each singly bonded atom hop, and 22,000 adatom hops occur for each doubly-bonded atom hop. Hence, a disproportionate amount of computation time is spent calculating adatom

dynamics. To reduce the disparity in rates, adatoms are allowed to make multiple nearest-neighbor hops, diffusing for *m* steps. The rate is scaled by a factor of *m*, giving a rate of 1/ *m* for each adatom hop in the series. An ideal step distance yields a time step that does not exceed the ratio of the rate of adatom hopping to the rate of the next fastest process.

To avoid the computational expense of allowing the adatom to perform an *m*-step random walk, which would require *m* random numbers, a search substitutes for a random walk. An approximate probability for finding a particle at the site (*i, j)* after an m^2-length random walk is given by

$$p_{i,j}^{t+m^2} = \frac{1}{4}(p_{i-m,j}^{t} + p_{i+m,j}^{t} + p_{i,j+m}^{t} + p_{i,j-m}^{t}). \quad (11)$$

This distribution contains only four potential new locations for the adatom. To simulate an m^2-length random walk, a square extending *m*-1 spaces on each side of the current site is searched for attachment sites, and then the adatom is moved *m* spaces in one of the four possible directions, which is chosen randomly. If attachment sites exist within the square, a step with fewer than *m* hops is taken. The process is repeated until *m* hops have been taken. If the adatom attaches, another adatom moves for the remaining portion of the time step.

The MSKMC algorithm yielded results in good agreement with the standard BKL algorithm over both short and long-term simulations, and MSKMC simulations ran between six and seven times faster than BKL simulations. This improved efficiency was attributed to the fact that the local searches required by the MSKMC algorithm to simulate *m* adatom hops were less computationally

demanding than the generation of *m* random numbers, even when a relatively fast random number generator was employed. Use of a slower random number generator would likely have amplified the efficiency gains made using the MSKMC algorithm.[37]

3.5 Multi-step Kinetic Monte Carlo Simulations in Perovskite Systems

The earliest applications of KMC simulation to the problem of conduction pathway determination have focused on transitions from one state to the next corresponding to a single proton transition at each iteration of the algorithm.[9,10] Ciszewski recently developed a multi-step KMC algorithm that instead considers a series of state transitions corresponding to the proton's movement along an *n*-step pathway at each iteration.[38] In contrast to the system described in the previous section, the perovskite systems allows only one type of transition—movement from a state with the proton bound in one site to a state with the proton in a different site—and transition events occur on a single timescale. Like the multi-scale algorithm, though, the multi-step algorithm was aimed at increasing computational efficiency by decreasing the number of times random numbers must be generated in order to select moves. In the multi-step algorithm, all possible *n*-step pathways from each site in the system are generated using the graph theoretical methods described in Section 4.2 during pre-simulation calculations. When the simulation begins and a move must be made, a random

number is drawn to select a pathway accessible from the current binding site using the linear search method. Both the multi-scale and multi-step algorithms employ a single random number rather than *n* random numbers at this stage, but the multi-step algorithm, designed for a simpler system, does not require the spatial search the multi-scale algorithm employs as a means of simulating a random walk. A pre-defined random walk is simply selected at random.[38]

Ciszewski's algorithm stopped short of providing a method for calculating rate constants for multi-step moves. Following de Vita and coworkers,[37] the algorithm was altered so rate constants for each single move making up an *n*-step pathway were totaled and scaled by the number of steps in the pathway to give the rate constant for the path according to the equation

$$k_{path} = \frac{\sum_{i=1}^{n} k_i}{n} \tag{12}$$

where n is the number of steps in the pathway and k_i is the rate constant for a single step in the pathway. Path speed is inversely proportional to path length. This method of rate constant calculation is justified by the fact that an ensemble of independent Poisson processes behaves as a single Poisson process, and its properties can be determined by reference to the properties of the individual processes.[35] In this case, since each step along a pathway is the result of a Poisson process, the entire pathway can be treated as a larger Poisson process, and a rate constant for the pathway can be generated from rate constants for the single steps.

3.6 Results from the Multi-step KMC Algorithm in Doped Perovskite Systems

This novel multi-step algorithm was first tested in the undoped bulk $BaZrO_3$ system, where two to three-step pathways were determined to give optimal computation times.[38] In this study the multi-step simulation method was applied to three representative doped perovskite systems: Al-doped $SrZrO_3$, Y-doped $SrZrO_3$, and Y-doped $BaZrO_3$. Conduction pathways yielded by the simulations in each system were in good agreement with pathways generated using standard single-step KMC simulations and graph theoretical methods. The same pathway through the Al-doped $SrZrO_3$ system illustrated in Figure 3.2 is shown below in Figure 3.3 as a composite of shorter pathways generated in a multi-step simulation with $n = 2$.

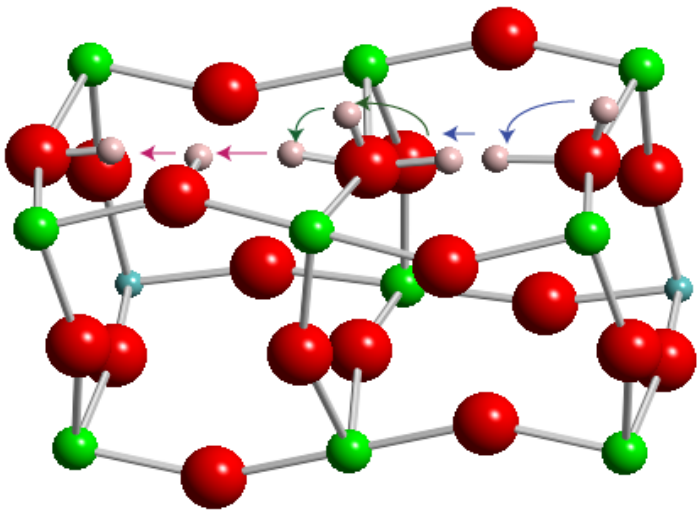

Figure 3.5 Another illustration of the most probable conduction pathway in the Al-doped $SrZrO_3$ system. Here, the short two-step pathways that were chosen during the simulation are highlighted in different colors.

Moreover, the average times spent by the proton at each binding site during the simulations, the average residence times, matched average residence times for single-step KMC simulations. This suggests that the method for calculating k_{path} yields accurate values, as inaccurate values would skew the length of time steps chosen (see Equation 2).

Simulation program runtimes show that using n-step moves at each iteration of the algorithm does increase computational efficiency for $n = 2$ and $n = 3$. For each system and value of n (ranging from one to five), ten simulations were performed for each of three trajectory lengths (one, two, and three million picoseconds). Simulations were performed at 600 K. The run times for each set of simulations were averaged to evaluate the performance of algorithms with different n values in each system for different trajectory lengths. Averages obtained for the Al-doped $SrZrO_3$ system, system are shown below in Figures 6. Figure 3.6 also shows average run times for the single-step KMC program for comparison. Simulations run in other bulk perovskite systems yielded similar results.

The results reflect competing efficiency effects at play in the multi-step algorithm. For short pathways, it is apparent that reducing the number of move choices that must be made to simulate the total trajectory time increases program efficiency. This is to be expected, as the process of selecting a move requires the generation of a random number and an array search. However, for pathways longer than three steps, the computational cost of generating and storing every

possible pathway begins to outweigh the time saved by making fewer move choices.

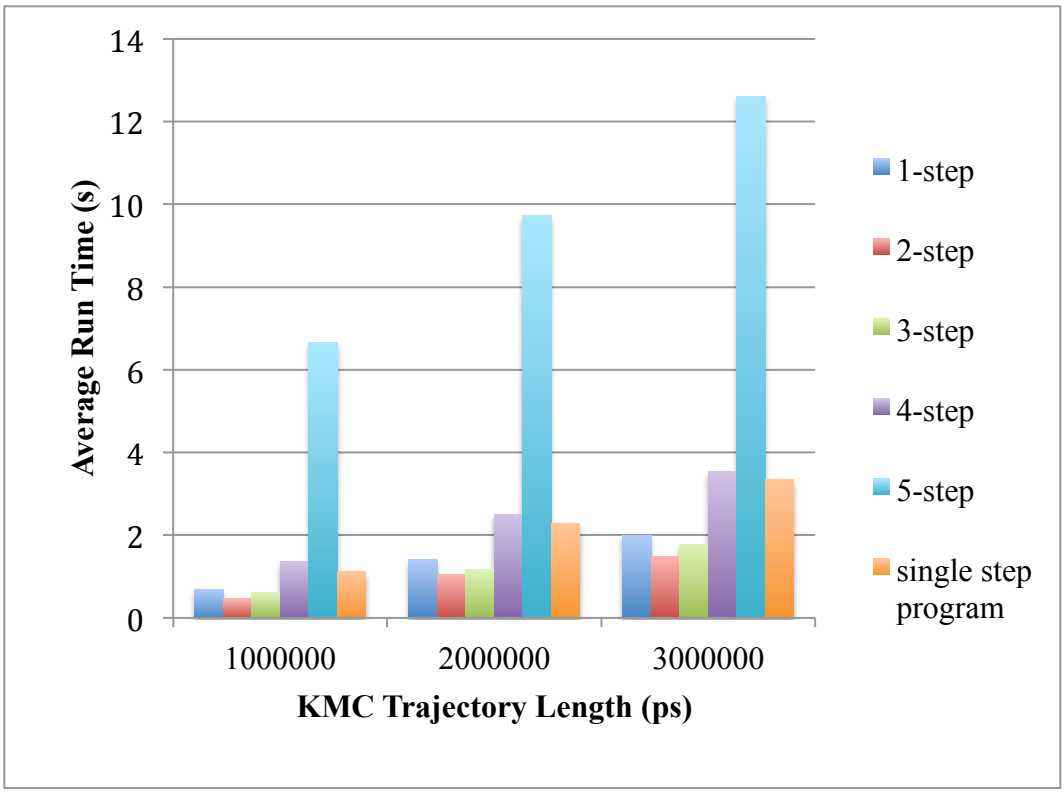

Figure 3.6 Run times for KMC simulations in the $AlSrZrO_3$ system with three different trajectory lengths. Notice that the optimal pathway length is two steps. As the pathway lengths increase beyond three steps, run times begin to increase as the savings associated with making fewer move choices are outweighed by the cost of generating and storing longer pathways.

3.7 Conclusions

The novel multi-step KMC algorithm yielded conduction pathways in good agreement with pathways generated using a simpler KMC algorithm. It was demonstrated that using multi-step pathways with $n = 2$ or $n = 3$ allowed the program to run more efficiently than use of single steps within the multi-step algorithm or single steps within the single step algorithm. The time saved by using short pathways increased as the trajectory lengths increased, suggesting that the multi-step algorithm would prove particularly valuable when long trajectories are required.

Chapter 4

Extending Graph Theory Analysis to Understand Relationships Between Binding Sites in Perovskite Systems

From its beginnings in Euler's 1736 mathematical formulation of the Königsberg Bridge Problem,[40] graph theory has evolved into a complex, multi-disciplinary field of inquiry. Graph theory has been applied to problems ranging from protein structure prediction[41] in the biological realm to evaluation of consistency of choice in psychology and percolation processes in physics.[42] This chapter will present essential graph theory definitions and discuss prior use of graph theory in determining conduction pathways in perovskites. Further, it will describe a novel application of a graph theoretical method of evaluating binding site centrality aimed at clarifying the relationships between binding sites and the flow of protons in perovskite systems.

4.1 Graph Theory Definitions

A graph G consists of a finite, non-empty set of vertices $V(G)$. A set of unordered pairs of distinct vertices is known as the edge set $E(G)$. Any two vertices u and v that form one of these pairs are joined by some edge $e = \{u, v\}$ and are described as adjacent vertices. Adjacency relationships between vertices $\{v_1, v_2, \ldots, v_p\}$ may be described by a symmetric p x p adjacency matrix $A(G)$ with entries a_{ij} such that

$$a_{ij} = \begin{cases} 1 \text{ if } v_i v_j \in E(G) \\ 0 \text{ if } v_i v_j \notin E(G) \end{cases}. \quad (1)^4$$

An example graph with the vertices $V(G) = \{v_1, v_2, v_3, v_4, v_5\}$ and the edges $E(G) = \{v_1v_4, v_1v_3, v_2v_3, v_2v_5, v_3v_4, v_3v_5\}$ is shown in Figure 4.1 with its adjacency matrix.

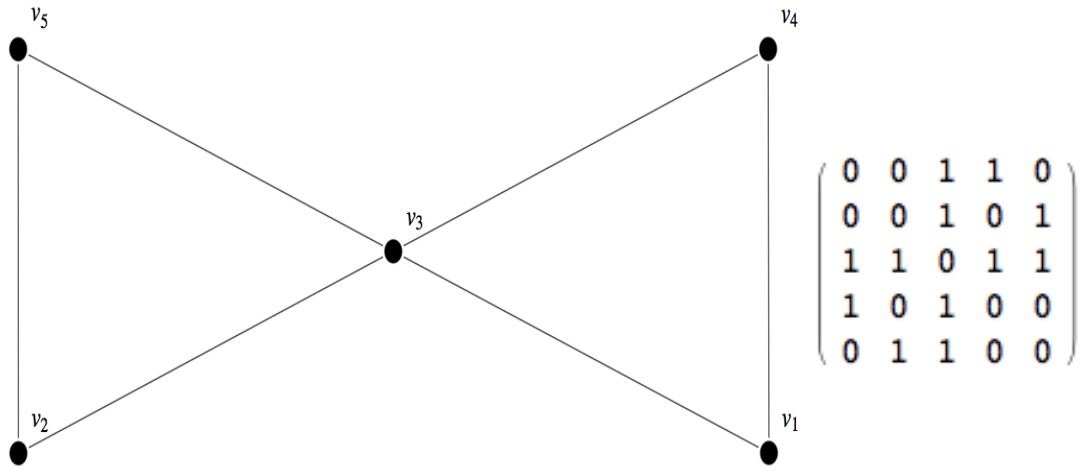

Figure 4.1 Graph and adjacency matrix representations of a graph with the edges and vertices described above. Vertices in graphs are typically represented as points, and edges are represented as lines.

A directed graph or digraph D consists of a non-empty, finite set of vertices $V(G)$, but in contrast to the vertices of graphs, the vertices of digraphs may be joined by arcs or directed edges, where the arc set $E(D)$ consists of sets of ordered pairs of vertices. Figure 4.2, below, illustrates a digraph with the vertices $V(D) = \{v_1, v_2, v_3, v_4, v_5\}$ and the directed edge set $E(D) = \{v_1v_3, v_2v_3, v_2v_5, v_3v_1, v_3v_2, v_4v_1, v_4v_3, v_4v_5\}$. The edges of a graph or digraph may each be assigned a positive real number, in which case the graph or digraph is weighted.

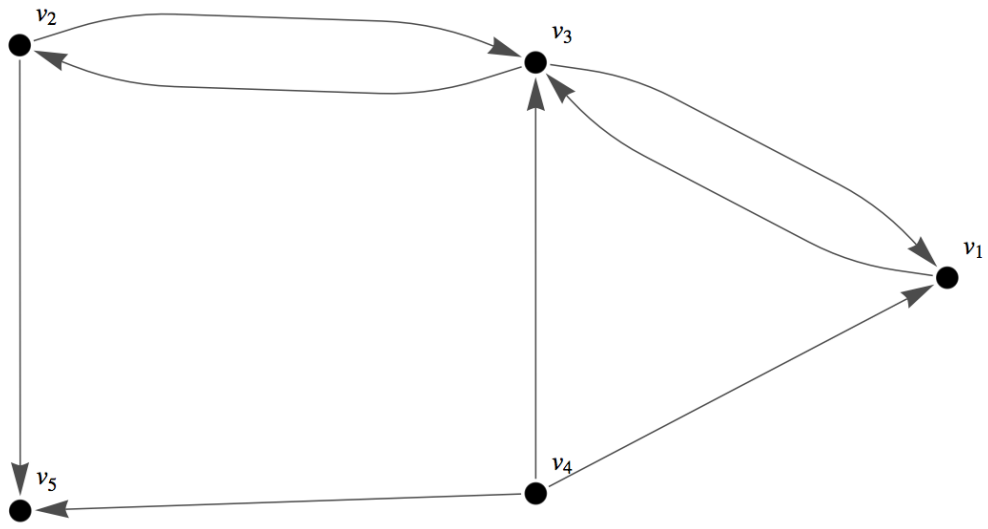

Figure 4.2 The sample digraph described above. As with graphs, vertices are represented as points. Directed edges are represented as rays.

If u and v are vertices of a digraph, a u-v walk consists of a finite, alternating sequence of vertices and edges of the form $u = u_0, e_1, u_1, e_2, \ldots, u_{n-1}, e_n, u_n = v,$ beginning with vertex u and ending with vertex v such that $e_i = u_{i-1}u_i$ for $i = 1, 2, \ldots, n$. A u-v walk in which no vertices are repeated can be described as a

u-*v* path. When a digraph *D* contains a *u*-*v* path, we say vertex *v* is reachable from vertex *u.* For every two distinct vertices of *D*, if each is reachable from the other, the digraph is described as strongly connected.[43]

4.2 Modeling Perovskite Systems as Digraphs for Pathway Determination

In the past, Y and Al-doped $SrZrO_3$ and Y-doped $BaZrO_3$ bulk systems have been modeled as digraphs in order to generate possible *n*-step periodic conduction pathways. Each vertex in the graph corresponds to one of the 96 proton binding sites, and each edge corresponds to a transition state connecting neighboring binding sites. The digraph representing the Y-doped $BaZrO_3$ system is illustrated below in Figure 4.3.

Dynamic programming is used to determine all possible pathways of a certain length that span the system by connecting a binding site to its periodic image. To allow paths to be sorted by probability, each edge e_{ij} is assigned a positive weight w_{ij} equal to -ln(p_{ij}), where p_{ij} is given by Equation 3 in Chapter 3. The total weight for an *n*-step pathway from some site *j* to its periodic image, then, is given by

$$w = -\ln(\rho_{j_1}) + \sum_{i=1}^{n} w_{j_{i-1},j_i} \qquad (2)$$

where ρ_{j1} is the probability of the proton occupying site *j*.

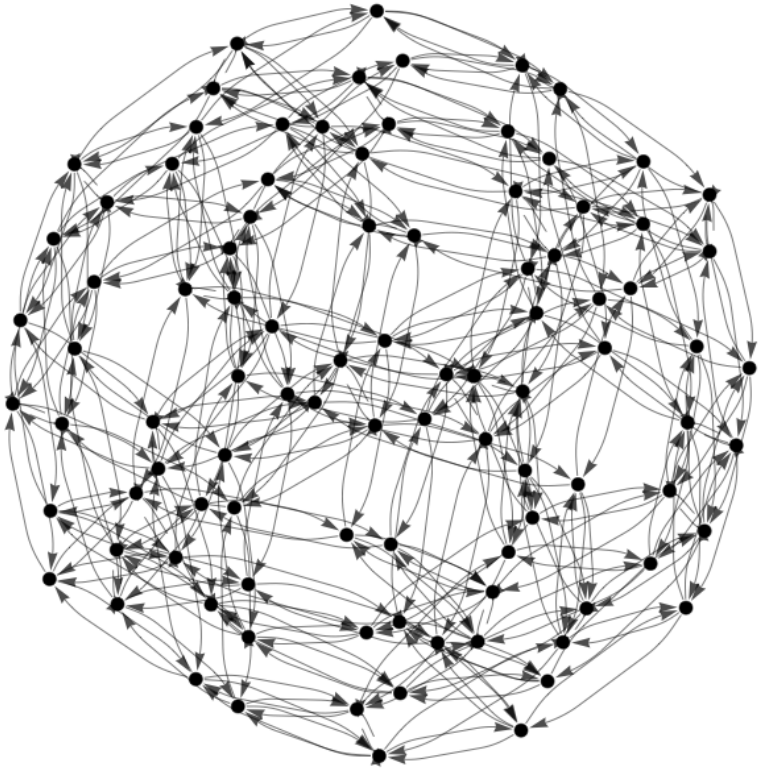

Figure 4.3 A digraph representation of the Y-doped $BaZrO_3$ system. This representation reflects the connections between vertices, but the lengths of the rays do not correspond to the weights of the directed edges.

The highest-probability paths have the lowest weights. Total path weights rather than total path probabilities are used in ranking path probability because weights may be summed over the pathway to calculate total weight, whereas calculating a total path probability would require multiplication of probabilities at each step of the pathway, a more expensive calculation. Pathways and relative probabilities determined using the digraph model have been in good agreement with pathways found using kinetic Monte Carlo simulations (See Chapter 3).[9,10,44] The probability of transition from some site *i* to another site *j* is different than the

probability of transition from j to i, so it is appropriate to model the systems as digraphs rather than graphs, because each directed edge connecting v_i to v_j may be given a different weight. In every case, though, if a directed edge e_{ij} connects v_i to v_j, another directed edge e_{ji} connects v_j to v_i.

4.3 Evaluating the Centrality of Vertices in Graphs and Digraphs

Development of methods for determining the relative centralities of vertices in graphs is one of the key problems in the field of network analysis. Broadly, a vertex's centrality can be understood as its contribution to the graph. Freeman (1978) suggested that centrality should be intuitively understood as the quality possessed by a vertex at the center of a star-shaped graph or in the hub position of a wheel-shaped graph.[45] A more precise definition for centrality may be formulated based on the system the graph represents. For example, if a graph is used to model connections within a social network, with each vertex corresponding to an individual, a high centrality ranking for a vertex would indicate that the corresponding individual is highly influential or is in a position to control the flow of information in the group.[45,46]

Evaluating the centralities of vertices in the digraphs representing the perovskite systems seemed a natural extension of prior graph theoretical analysis. In this section, the three common centrality measures formalized by Freeman will be presented, and their applications, limitations, and potential for measuring

centrality in perovskite systems will be discussed. The limitations of each basic method have served to motivate the use of a centrality measure for digraphs representing perovskite systems based on an understanding of the digraphs as representations of Markov chains. This measure will be introduced in the next section.

4.3.1 Degree Centrality

The degree of some vertex v_i in a graph is equal to the number of edges connecting v_i to other vertices, or the number of ordered pairs containing v_i. It is apparent that vertices forming the centers of wheel or star-shaped clusters generally have higher degrees than surrounding vertices. Hence, the simplest measures of degree centrality simply take vertices with higher degrees to be more central.[45] By this measure, v_3 (degree = 4) would be the most central vertex in the graph displayed in Figure 4.1. When the graph in question is weighted, the degree centrality (known as node strength in the case of weighted graphs) of a vertex v_i may be given as the sum of the weights of the edges connecting v_i to other vertices, with higher values indicating higher centrality.[47] The concept of degree centrality has been applied in analysis of biological networks. While networks may be generally robust against random disturbances, it has been shown that disturbances at points corresponding to vertices with high degree centrality often bring about system failure.[48]

Despite their appealing simplicity, degree-based centrality measures convey a limited amount of information. They take only local structure into account. A vertex might be connected to a number of other vertices, or be connected by edges with high weights, but be relatively inaccessible from other areas of the graph.[49] As centrality analysis of the perovskite systems is aimed at improving understanding of pathways spanning the system, a global rather than local centrality measure is called for. Further, the vast majority of degree-based centrality measures have been formulated for graphs rather than digraphs, making them inappropriate for analysis of perovskite systems best represented by digraphs.

4.3.2 Betweenness Centrality

Another characteristic of vertices at the center of wheels or stars is that they lie along a number of the shortest paths connecting non-adjacent vertex pairs (pairs of vertices that do not share an edge).[45] For an unweighted graph, a simple measure of the betweenness centrality of a vertex v_i is given by

$$C_b(v_i) = \sum_{\{(v_j, v_k) | v_i \notin (v_j, v_k)\}} \frac{\sigma_{jk}(i)}{\sigma_{jk}}, \qquad (3)$$

where $\sigma_{jk}(i)$ is the number of shortest paths connecting distinct vertices v_j and v_k that include v_i, and σ_{jk} is the total number of shortest paths connecting v_j and v_k. In the graph shown in Figure 4.1, v_3 has the highest betweenness centrality. Betweenness centrality has been applied to graphs representing protein systems.

Proteins corresponding to vertices with high betweenness centrality have been shown to play important functional and dynamic roles as connectors.[48]

Efforts have been made to develop formulations of betweenness centrality for weighted graphs, and betweenness centrality captures global characteristics to a greater degree than degree centrality.[49] However, the perovskite systems are uniform enough that large groups of vertices have the same levels of betweenness centrality, so this type of centrality measurement does not contribute to our understanding of binding site relationships in perovskite systems.

4.3.3 Closeness Centrality

Intuitively, vertices from which other vertices are easily accessible seem to play a greater role in their graphs. A simple calculation of closeness centrality for a vertex v_i in an unweighted graph involves adding the lengths of the shortest paths from v_i to each of the other vertices and taking the inverse of this sum. By this measure, v_3 has the highest centrality of the vertices in the graph shown in Figure 4.1. For weighted graphs, the sums of the edge weights in the each path replace path lengths. Applications of closeness centrality include identification of important metabolites in metabolic networks.[48]

4.4 A Centrality Measure Based on Expected Hitting Time

To develop a broader centrality measurement for the perovskite system graphs, it seemed desirable to evaluate the accessibility of a vertex v_i by considering all possible paths from other vertices to v_i, not merely the shortest ones taken into account by measures of closeness centrality. The general accessibility of one vertex from another may be given in terms of expected hitting time. When we consider a random walk over a diagraph, we can think of each vertex as a possible state of the system, and each movement from one vertex in the sequence to another vertex connected to the first by a directed edge as a state transition. Because the probability of a given transition depends only on the state the system currently occupies, not the system's past behavior, the series of states represented by the vertices visited during a random walk forms a Markov chain. The average number of transitions required to reach the state corresponding to vertex v_j (state j) from the state corresponding to another vertex v_i (state i) is termed the expected hitting time from v_i to v_j ($H(i,j)$),[49] or mean first passage time.[50]

To calculate hitting times for vertices in any digraph of interest, we must first develop a means of organizing the relevant probabilities. The probability distribution for all possible states in the system is given by the stationary probability vector $\boldsymbol{\pi}$. The ith component of $\boldsymbol{\pi}$ represents the probability that if an initial state for the system is chosen randomly, state i will be chosen. The entries

of $\boldsymbol{\pi}$ are positive and have a sum of one. For the perovskite systems, the entries of $\boldsymbol{\pi}$ consist of normalized Boltzmann factors:

$$\pi_i = \frac{e^{-\beta E_i}}{\sum_j e^{-\beta E_j}}, \tag{4}$$

where $\beta = \frac{1}{k_b T}$ and E_i is the energy of the system when it occupies a state with the proton bound at site *i*.

The probabilities of every possible transition from one state to another are given by the probability transition matrix **P**, whose entries p_{ij} give the probability of transition from state *i* to state *j*. For the perovskite systems, the entries p_{ij} represent the probability of the proton transitioning from a binding site *i* to another binding site *j*. They may be calculated using equation (3) given in Section 3.3. Diagonal entries p_{ii} are equal to zero.

In an intermediate step, we use $\boldsymbol{\pi}$ and **P** to form a new matrix **Z**, the fundamental matrix of the digraph. The inverse of the fundamental matrix for a digraph of *n* vertices representing a system with *n* possible states is given by

$$\mathbf{Z}^{-1} = \mathbf{I} - \mathbf{P} + \boldsymbol{\pi}, \tag{5}$$

where **I** is the *n* x *n* identity matrix.

The entries of **Z** in combination with the entries of $\boldsymbol{\pi}$ allow us to calculate the expected hitting time $H(i,j)$ from vertex v_i to vertex v_j:

$$H(i,j) = \frac{z_{jj} - z_{ij}}{\pi_j}. \tag{6}$$[50]

Summing over hitting times from every vertex v_i to a certain vertex v_j gives yields the total hitting time for vertex v_j, our chosen centrality measure:

$$H(j)_{total} = \sum_i H(i,j). \tag{7}$$

Lower total hitting times correspond to higher vertex centrality.

White and Smyth developed a similar centrality measure based on average hitting time. Termed Markov centrality, this measure considers the inverse of the average average hitting time from each of n vertices in the graph to the vertex of interest. The Markov centrality C of a vertex v_j is given by

$$C_j = \frac{1}{\frac{1}{n}\sum_i H(i,j)}. \tag{8}$$

In this case, higher values correspond to higher centrality.[51]

4.5 Hitting Time Centrality for Perovskite System Graphs

Each perovskite system's probability transition matrix **P** was constructed using probabilities calculated at 900 K. A stationary probability vector $\boldsymbol{\pi}$ was constructed for each system using energies calculated using DFT (see Chapter 2). The fundamental matrix for each system was then constructed according to Equation 6, and total hitting times for vertices corresponding to each binding site in each system were calculated using Equation 7. Although total hitting times were used to rank centrality, Markov centrality values would have produced equivalent rankings.

4.5.1 Hitting Time Centrality in the Al-doped $SrZrO_3$ System

Hitting time centrality was evaluated from each vertex in the graph representing the Al-doped $SrZrO_3$ system as described above. In Figure 4.4, below, the system is shown with a proton occupying each possible binding site. Protons are colored to reflect the centrality of the vertices corresponding to their binding sites.

It has been determined that the most probable pathways in the $AlSrZrO_3$ system tend to avoid the dopant. This trend is attributed to the relatively high energy barriers to interoctahedral transfers from binding sites near the dopant to binding sites farther away that serve to make paths traversing the dopant region less probable.[9] Thus, we would expect the binding sites that can be reached by interoctahedral transfer from a site on an oxygen adjacent to the dopant to be least accessible and have relatively low hitting time centrality. This is the case. The 22 least central binding sites in the system are all connected to sites adjacent to the dopant by interoctahedral transfers. The six most central sites, on the other hand, are located on oxygens as far away from the dopant as possible.

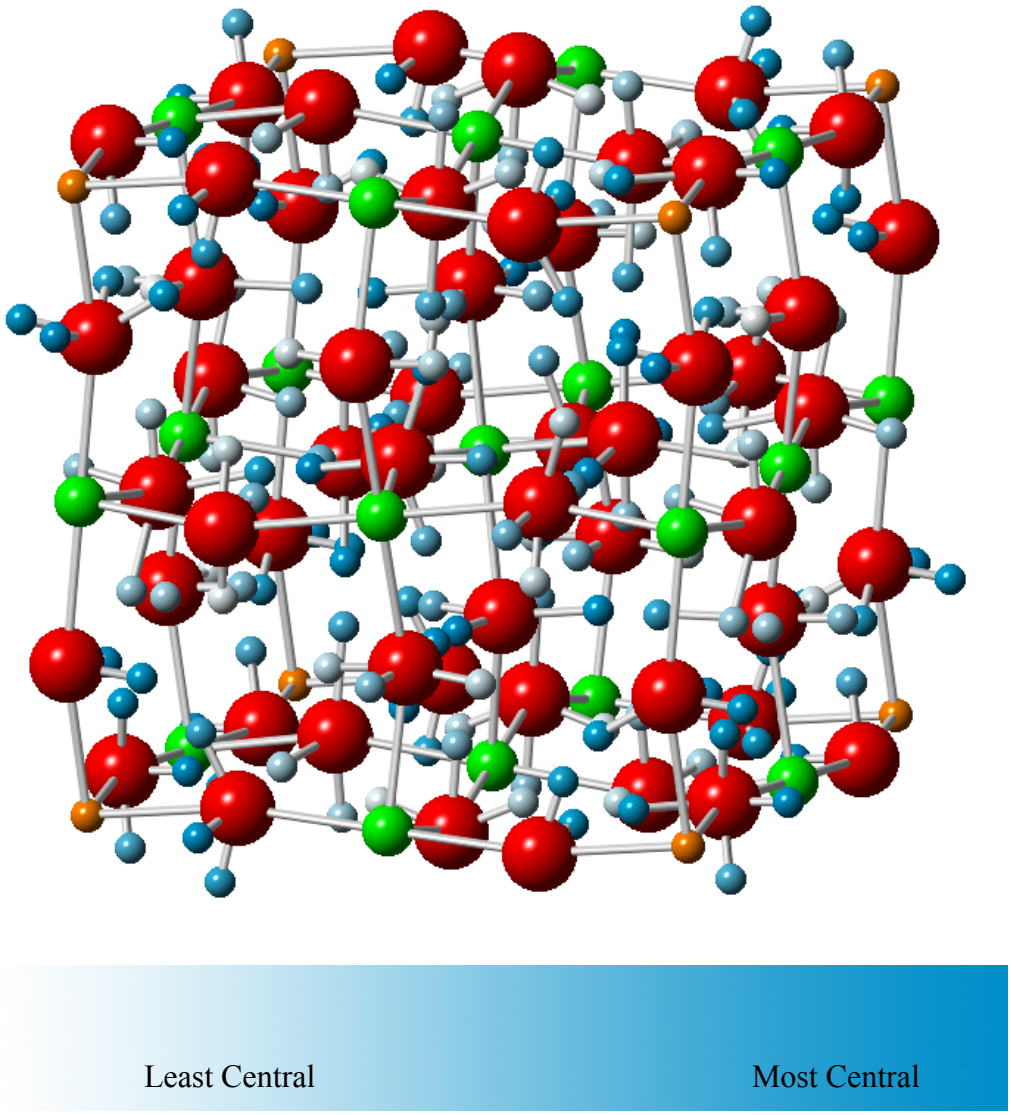

Figure 4.4 The binding sites of the $AlSrZrO_3$ system are shown occupied by protons color-coded by centrality as shown in the spectrum. For clarity, aluminum dopant ions are shown in orange. Notice that the least central sites are separated by interoctahedral transfers from sites on oxygens adjacent to the dopant, while the most central sites are located in the center of the system, as far as possible from the dopant.

Figure 4.5 shows the centrality of sites located along the most probable seven-step periodic conduction pathway in the system. The relative centralities of sites along the pathway vary, but the path does include the most central site in the system.

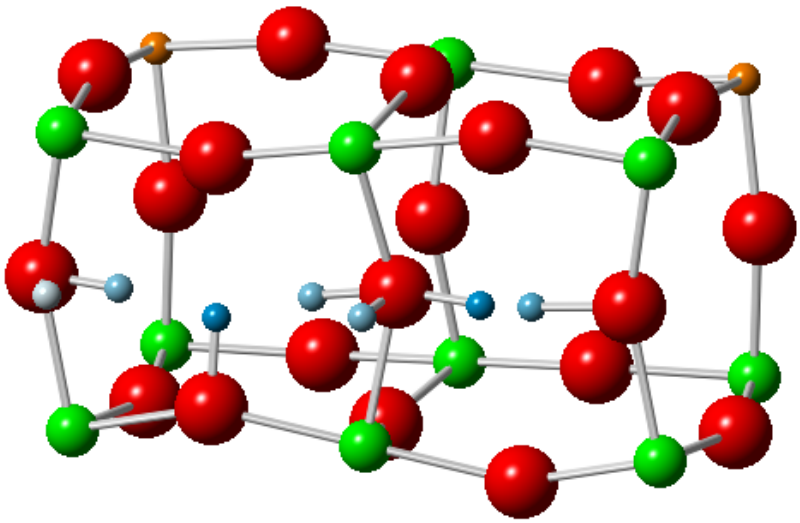

Figure 4.5 Protons are shown occupying each site in the most probable seven-step periodic conduction pathway in the $AlSrZrO_3$ system. The proton occupying the periodic image of the first site is not shown. The most central site in the system appears third from left and takes part in two transfers. The fifth most central site appears second from right and takes part in an interoctahedral transfer and a rotation.

4.5.2 Hitting Time Centrality in the Y-doped $SrZrO_3$ System

Binding sites in the $Y/SrZrO_3$ system were ranked by hitting time centrality as in the $AlSrZrO_3$ system. The results are shown in Figure 4.6.

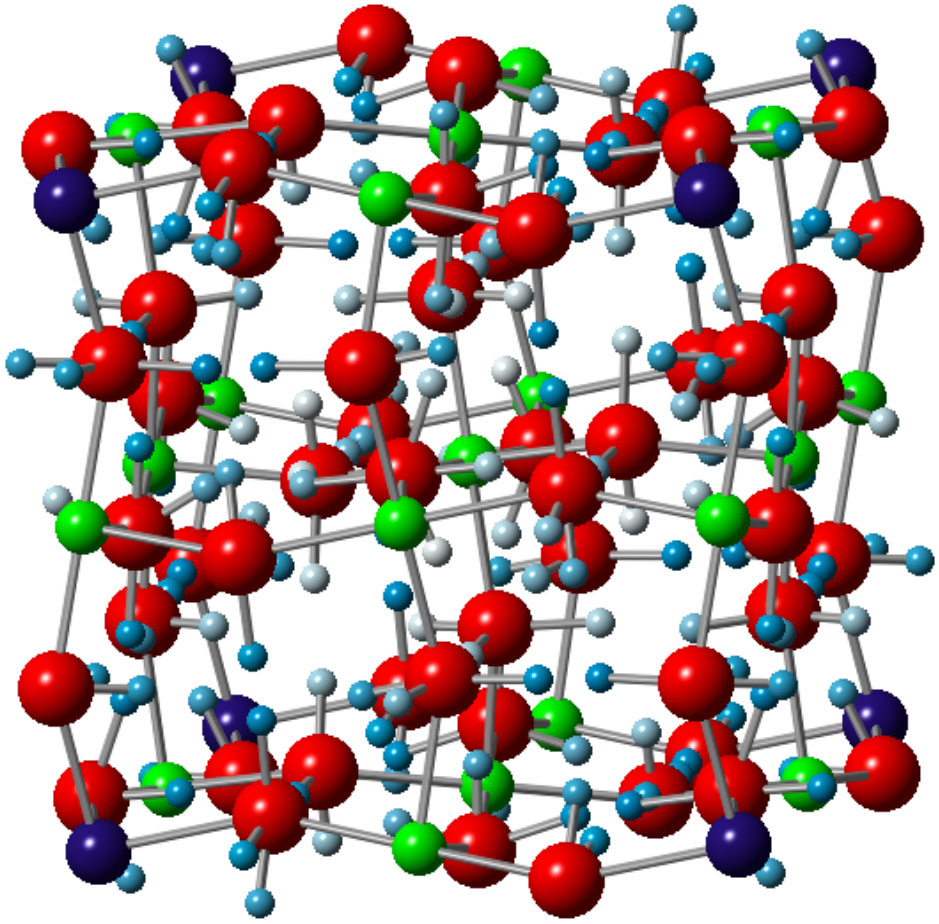

Figure 4.6 The Y/$SrZrO_3$ system is shown with protons occupying each binding site. Protons are color-coded by the centrality of their binding site as in Figure 4.4. Notice that the most central sites are located on oxygens adjacent to the dopant, whereas the least central sites are located on oxygens as far as possible from the dopant.

The high barriers to interoctahedral transfers away from oxygens adjacent to the dopant that characterized the Al $SrZrO_3$ system are absent in this system, and the most probable conduction pathways tend to traverse the dopant region.[9] In

contrast to the Al-doped system, then, we would expect the most central sites to occur on oxygens located adjacent to the dopant, and in fact the seven most central sites are located in this position. Sites separated from sites adjacent to the dopant by interoctahedral transfers are much more central than sites in the same position in the Al-doped system, which reflects their relatively greater accessibility. Sites along the most probable pathway in the system are shown below in Figure 4.7. This pathway includes the most central site in the system, and in general the sites along it have higher relative centrality than the sites along the most probable pathway in the Al-doped system. The presence of trajectories of more easily accessible sites in the $Y/SrZrO_3$ system seems consistent with the lower theoretically calculated average barriers to conduction in this system (0.43 eV vs. 0.61 eV in the Al-doped system).[9]

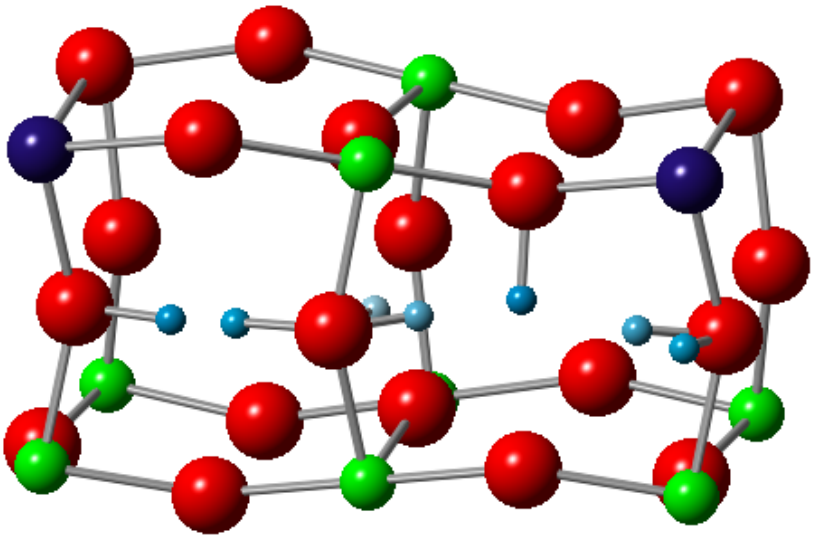

Figure 4.7 The most probable 7-step periodic conduction pathway in the $Y/SrZrO_3$ system. Again, the periodic image of the first site in the pathway is not shown. The most central site in the system appears third from right. Notice that the sites along this pathway are generally more central than the sites along the most probable pathway in the $AlSrZrO_3$ system.

4.5.3 Hitting Time Centrality in the Y-doped $BaZrO_3$ System

When hitting time centralities were evaluated for the $Y/BaZrO_3$ system, the patterns observed were relatively similar to the ones present in the $Y/SrZrO_3$ system (see Figure 4.9). The eight most central sites are located on oxygens adjacent to the dopant, and the least central sites are located on oxygens as far from the dopant as possible. This trend is consistent with the fact that the most probable paths in the system tend to avoid the region in the center of the simulation box far away from the dopant.[10]

The most probable seven-step periodic pathway, shown in Figure 4.8, does not include the most central binding site. It does, however, include the second and fourth-most central binding sites, and it shows a general centrality pattern similar to that of the most probable pathway in the Y-doped $SrZrO_3$ system. Again, the availability of high-centrality pathways seems to correspond to a lower conduction barrier. The overall barrier to conduction in this system is estimated to be 0.3 eV,[10] the lowest barrier among all the systems considered.

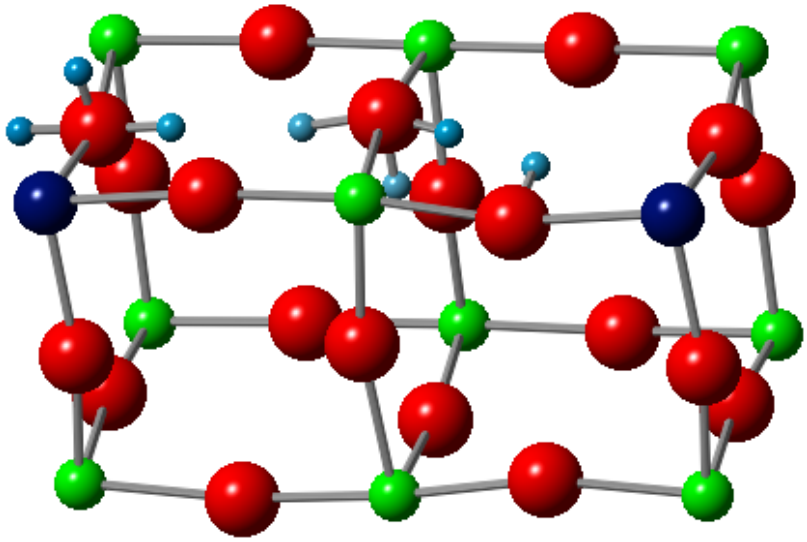

Figure 4.8 The most probable 7-step conduction pathway in the $Y/BaZrO_3$ system are illustrated below. The second most central site in the system appears on the left, and the fourth most central site appears second from left. Sites in the pathway generally have moderate to high centrality, as in the $Y/SrZrO_3$ system.

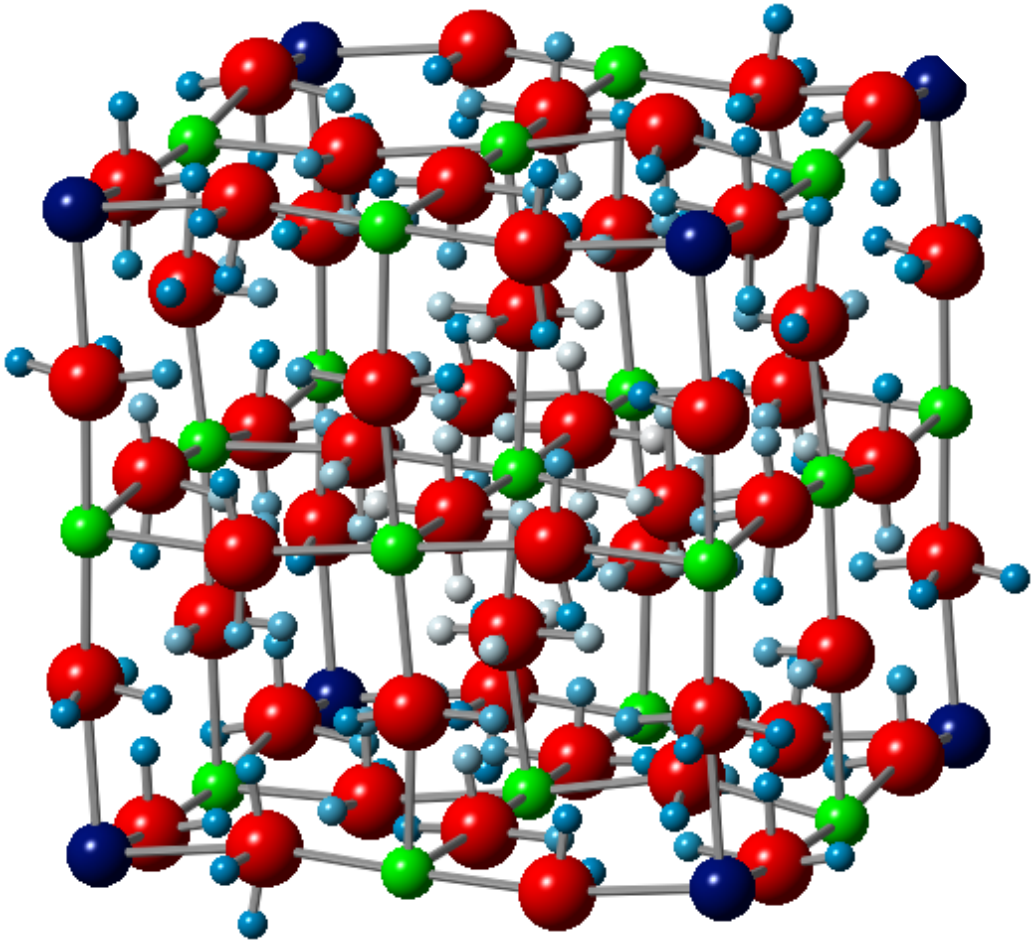

Figure 4.9 Protons are shown occupying each binding site in the Y/$BaZrO_3$ system. The least central sites are uniformly located on oxygens in the center of the simulation box, whereas more central sites appear in the dopant layers, particularly on oxygens adjacent to the dopant. The overall pattern is similar to the one displayed by the Y/$SrZrO_3$ system, despite the fact that the Y/$SrZrO_3$ system is significantly more distorted than the Y/$BaZrO_3$ system.

4.5.4 Hitting Time Centrality Patterns in the Al-doped $BaZrO_3$ System

Because the Al-doped $BaZrO_3$ system's cubic structure is significantly less distorted than the structures of the other perovskite systems, its conduction pathways are markedly different from the paths described in the other systems. In the other systems, distortions bring certain binding sites closer together, allowing interoctahedral transfers to occur between a number of sites. Depending on whether a site may participate in an interoctahedral transfer, each site is connected to four or five other sites by a single transition state. Interoctahedral transfers allow the proton to move in a single step to a site that would normally be reachable only by a two-step pathway consisting of a rotation and an intraoctahedral transfer, making it possible for the proton to travel the length of the simulation box in seven steps.[52]

In the Al-doped $BaZrO_3$ system, the lack of distortion prevents interoctahedral transfers from occurring. Each site is connected to exactly four other sites by single transition states, and the shortest paths spanning the simulation box are eight steps in length.[52] Because of these differences, we would expect to see distinctive trends in binding site accessibility in the Al-doped $BaZrO_3$ system. Hitting time centralities for each binding site are highlighted below in Figure 4.10. The general distribution of highly central sites does bear some resemblance to the Al-doped $SrZrO_3$ system. Highly central sites tend to be clustered in the inner octahedron and adjacent to the dopant in both systems.

However, while the most central sites in the $AlSrZrO_3$ system appear in the inner octahedron, the most central sites in the $Al/BaZrO_3$ system appear on oxygens adjacent to the dopant. Both Al-doped systems are marked by low binding energies adjacent to the dopant and thus high barriers to escape from these sites. Hitting time centrality patterns suggest, though, that sites adjacent to the dopant are more accessible in the $Al/BaZrO_3$ system than in the $AlSrZrO_3$ system. The 24 sites that are separated by intraoctahedral transfers from sites adjacent to the dopant in the $Al/BaZrO_3$ system and are not adjacent to the dopant themselves are the least accessible in the system.

In contrast to the most probable seven-step pathways in the other perovskite systems, the most probable eight-step conduction pathway in the $Al/BaZrO_3$ system (shown in Figure 4.11) does not include any highly central sites. As it runs through the center of the simulation box, as far from the dopant as possible, it avoids both the most central and the least central sites in the system. The least central site along the most probable pathway ranks 75^{th} of 96 in centrality, whereas the most probable pathway in the $AlSrZrO_3$ system includes the 89^{th} most central site in the system.

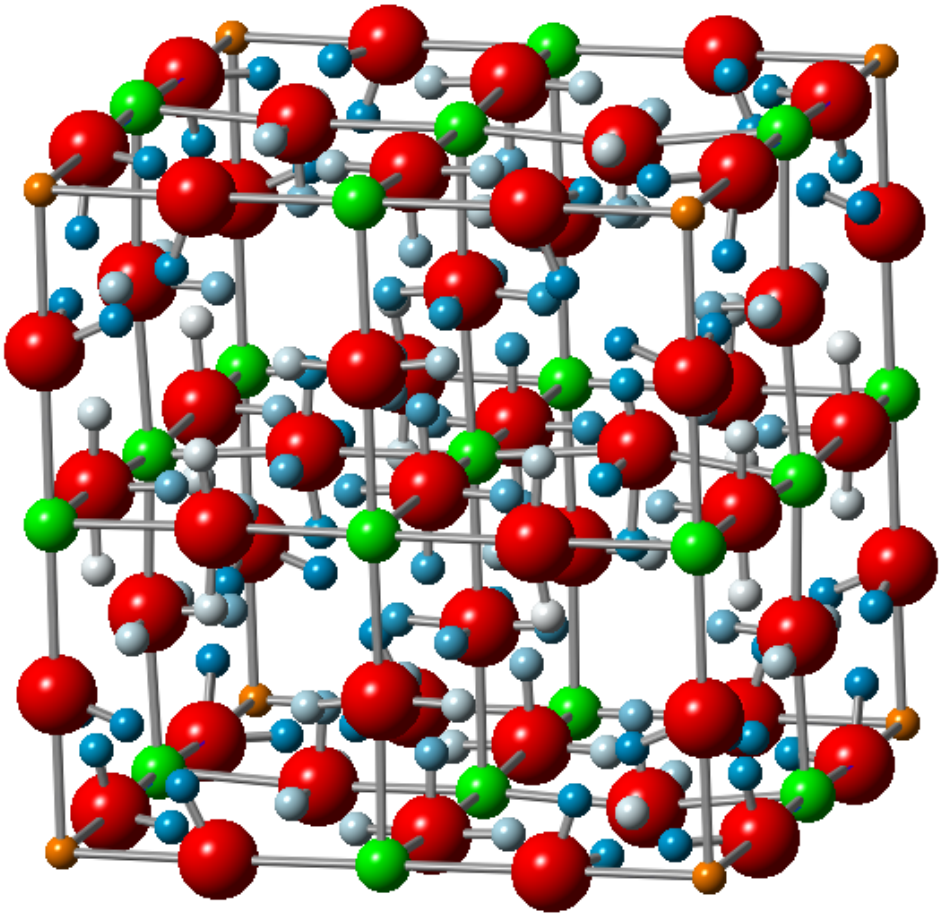

Figure 4.10 Each site in the Al/$BaZrO_3$ system is shown occupied by a proton colored to reflect its hitting time centrality. Notice that the most central sites in the system are located on oxygens adjacent to the dopant, while the least central sites are the ones reachable by intraoctahedral transfer from the most central sites.

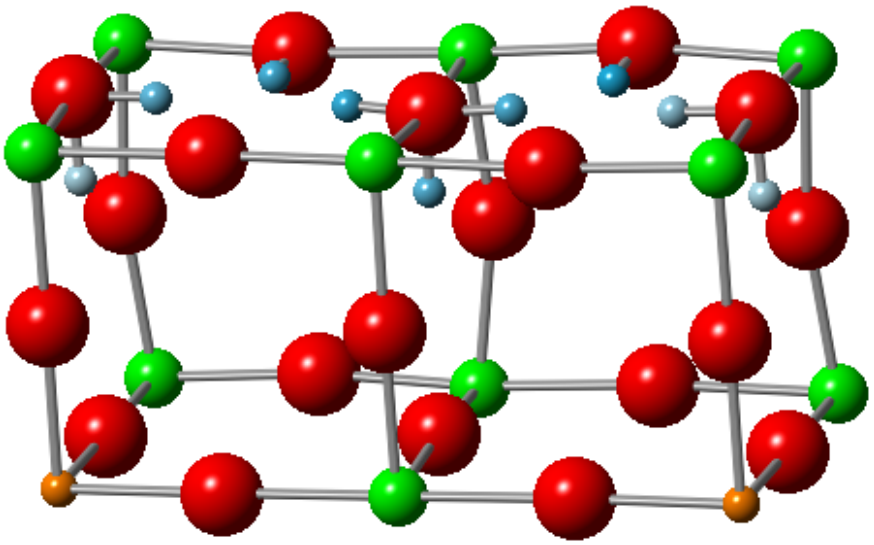

Figure 4.11 The most probable eight-step conduction pathway in the Al/$BaZrO_3$ system. Notice that in general, the sites have lower centralities than sites along the most probable seven-step pathways in the other perovskite systems.

The lower centrality of the sites along the most probable pathway in the Al/$BaZrO_3$ system relative to the sites along the most probable pathway in the Y/$BaZrO_3$ system seems to be in keeping with the difference in barriers to conduction between the two systems. Theoretical estimates place the average conduction barrier at 0.41 eV for the Al-doped system[52] (as opposed to 0.3 eV for the Y-doped system).[10]

4.6 Site Centrality in Proton Traps

Up to this point, the only pathways that have been discussed are those spanning the systems' simulation boxes, stretching from a binding site to its periodic image.

It is important to remember that in the absence of an electric field, the proton's trajectory during a KMC simulation will include a number of loops. To shed light on these common features of proton conduction, the centralities of the binding sites along the most probable loops spanning more than 40 percent of the simulation box were evaluated for the Al/$BaZrO_3$ and Y/$BaZrO_3$ systems. Loops were generated from KMC trajectories run at 900 K. These loops are shown in Figures 12 and 13, respectively.

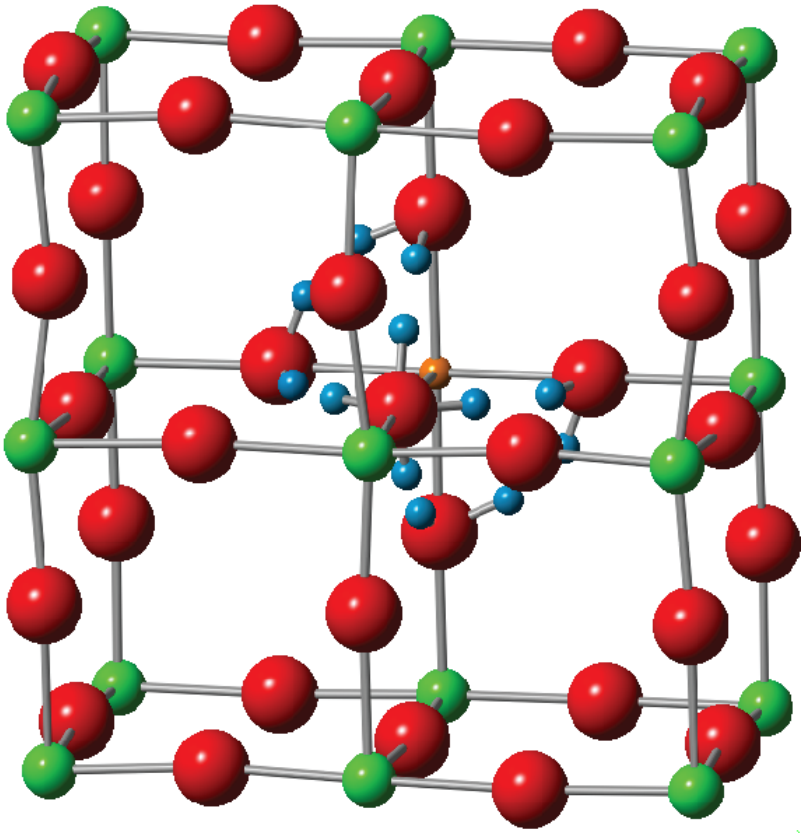

Figure 4.12 The most probable loop in the $AlSrZrO_3$ system. Notice that the sites are all above median centrality, and they cluster around the dopant. Comparison with Figure 4.10 shows that the sites surrounding the loop have low centralities.

The most probable loops in both systems comprise binding sites adjacent to the dopant. In each loop, every binding site ranks in the top 50 percent for centrality. The loop in the Y/$BaZrO_3$ system includes the most central binding site, and the loop in the Al/$BaZrO_3$ system includes the second, third, and fourth-most central binding sites in the system. Comparing the loops to the full rankings shown in Figures 9 and 10, the differences between the two systems become apparent. While the loop in the Y-doped system is surrounded by moderate-centrality sites, the loop in the Al-doped system is surrounded by very low-centrality sites. This suggests that the loop in the Y/$BaZrO_3$ system might be escaped without much difficulty, but the loop in the Al/$BaZrO_3$ system might function as a hard-to-escape proton trap. The presence of such traps in Al-doped systems might help explain the higher barriers to conduction in these systems.

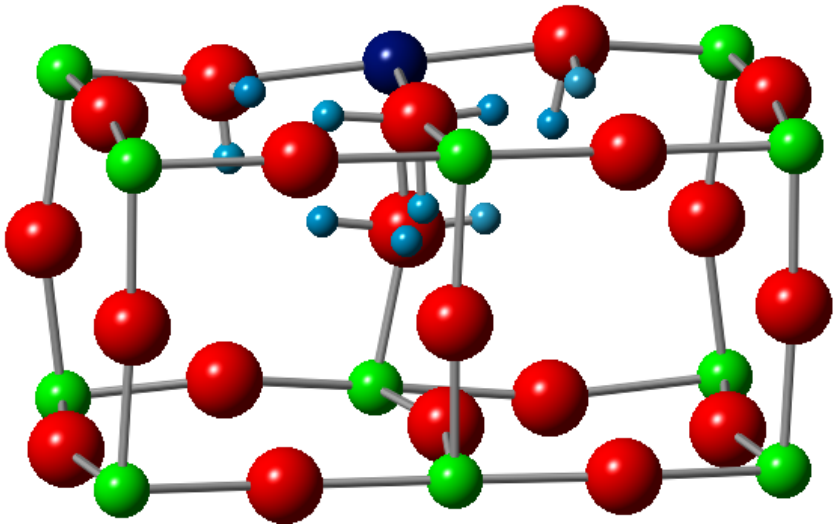

Figure 4.13 The most probable loop in the Y/$BaZrO_3$ system. It includes the system's most central site. The surrounding sites have moderate centralities.

4.7 Conclusions

Hitting time centrality provides a general means of determining which vertices in a graph are easily accessible from other vertices. Its treatment of the graph as a representation of a Markov chain allows it to capture variation in the importance of vertices and their corresponding states even for graphs that lack the wheel or star patterns that are intuitively associated with centrality, such as the graphs representing perovskite systems. When it is applied to the perovskite graphs, the resulting trends in binding site centralities appear to be consistent with observed patterns in site accessibility, locations of probable pathways, and overall barriers to conduction. Relative site centralities offer a new way of understanding these observed trends as well as information-rich snapshots of binding site relationships.

Chapter 5

Conclusions and Directions for Future Work

5.1 Toward Full Characterization of the 310 Tilt Grain Boundary System

This work has discussed the results of grain boundary optimizations using three exchange-correlation functionals and their associated pseudopotentials. Two 310 Y/$BaZrO_3$ grain boundary structures that differed in the placement of the dopant along the grain boundary core were minimized using each of the functionals. The PW91 and LDA functionals were shown to produce similar patterns of distortion and relative energies for the two structures, while the PBE functional yielded higher levels of distortion and reversed the trend in relative energies. Further characterization of the grain boundary will require the choice of one of these functionals for the remaining calculations. Recent theoretical explorations of Y/$BaZrO_3$ grain boundary structure have employed the PBE functional,[24,26] so use of this functional might improve the comparability of future results.

Once a functional has been selected, the structure with the dopant in the position that yielded the lowest energy configuration using that functional will be selected for continuing characterization. Structures with single protons in each of the possible binding sites in the system will be optimized to determine the binding energies for each site in the system. Next, barriers to transition between binding sites connected by transition states will be calculated using the nudged elastic band (NEB) method. Frequencies necessary for the calculation of prefactors for each of these transitions will also be determined.

Determination of binding energies, transition barriers, and prefactors will allow rate constants for each possible proton move to be calculated as described for bulk systems in Chapter 3. These rate constants will then be used in KMC simulations and the graph theoretical analysis process to extract long-range conduction pathways through the grain boundary and determine the activation energy for proton conduction through the grain boundary. Finally, the hitting time centrality of each site in the system will be evaluated as described in Chapter 4 to examine trends in the locations of high-probability conduction corridors and proton traps. It is expected that centrality analysis will yield particularly helpful insights in a grain boundary system with less regular patterns of connection between binding sites than the bulk systems.

5.2 Kinetic Monte Carlo Simulations

This work has described the implementation, testing, and fine-tuning of a multi-step KMC algorithm used to simulate proton conduction in bulk perovskite systems. It has been shown that choosing 2 or 3-step pathways at each iteration of the algorithm rather than single moves decreases program run time, and the computational savings increase as simulation trajectory times increases. It has also been demonstrated that a simple method of scaling the rate constants for each *n*-step pathway yields appropriate step rate constants and time steps. Pathways determined using the single-step and multi-step algorithms were found to be in good agreement. Minor alterations will be required to generalize the multi-step KMC simulation program for use in grain boundary systems. Additional alterations would allow the program to calculate diffusion constants for the proton in each system.

5.3 Increasing the Scope of Centrality Analysis

Chapter 4 described how a graph theoretical centrality measure based on average hitting time yielded insights into the relationships between binding sites in bulk perovskite systems and the likely flow of protons in these systems. Moreover, distributions of highly central sites help explain activation barriers within each system. Y-doped systems that display lower barriers to conduction are characterized by trajectories of highly central sites spanning the their simulation boxes, while the most central sites in Al-doped systems with higher barriers to

conduction are scattered across the simulation boxes. The regularity of the bulk systems made betweenness and degree centrality measures meaningless, but these measures might prove more useful in grain boundary systems, where the numbers of connections between each site and the weights of connecting edges in graphs are expected to be more varied. Together with KMC results, these centrality measures will help provide a rigorous characterization of the flow of protons in the 310 Y/$BaZrO_3$ tilt grain boundary system.

Bibliography

[1]United States Department of State, *U.S. Climate Action Report 2010* (Global Publishing Services, Washington, 2010), p. 5.
[2]V. S. Bagotsky, *Fuel Cells: Problems and Solutions* (Wiley, Hoboken, NJ, 2009).
[3]M. M. Mench, *Fuel Cell Engines* (Wiley, Hoboken, NJ, 2008).
[4]J. Wu *et al.*, Int. J. Hydrogen Energ. **33**, 1735 (2008).
[5]U.S. Department of Energy, "Types of Fuel Cells," 8 March 2011, http://www1.eere.energy.gov/hydrogenandfuelcells/fuelcells/fc_types.html (7 Feb. 2013).
[6]T. Norby, Nature **410**, 877 (2000).
[7]L. Malavasi, C. A. J. Fisher, and M. S. Islam, Chem. Soc. Rev. **39**, 4370 (2010).
[8]M. A. Peña and J. L. G. Fierro, Chem. Rev. **101**, 1981 (2001).
[9]M. A. Gomez, M. Chunduru, L. Chigweshe, and K. M. Fletcher, J. Chem. Phys. **133**, 064701 (2010).
[10]M. A. Gomez, M. Chunduru, L. Chigweshe, L. Foster, S. J. Fensin, K. M. Fletcher, and L. E. Fernandez, J. Chem. Phys. **132**, 214709 (2010).
[11]P. Lejcek, *Grain Boundary Segregation* (Springer, New York, 2010).
[12]T. Ishihara, in: *Perovskite Oxide for Solid Oxide Fuel Cells*, (Springer, New York, 2009).
[13]B. Merinov and W. Goddard III, J. Chem. Phys. **130**, 194707 (2009).
[14]R. Dohmen and R. Milke, Rev. Mineral. Geochem. **72**, 921 (2010).
[15]A. C. T. van Duin, *et al.* J. Phys. Chem. A **112**, 11414 (2008).
[16]P. Babilo, T. Uda, and S. M. Haile, J. Mater. Res. **22**, 1322 (2007).
[17]F. Iguchi, *et al.* Solid State Ionics **178**, 691 (2007).
[18]H. Ji, *et al.* Solid State Ionics **203**, 9 (2011).
[19]H. G. Bohn, T. Schober, J. Am. Ceram. Soc. **83** 768 (2000).
[20]R. B. Cervera *et al*. Solid State Ionics **179**, 236 (2008).
[21]J. Jamnik, J. Maier, and S. Pejovnik, Solid State Ionics **75**, 51 (1995).
[22]M. Shirpour, R. Merkle, and J. Maier, Solid State Ionics **216**, 1 (2012).
[23]C. Kjolseth *et al.* Solid State Ionics **181**, 268 (2010).
[24]E. E. Helgee, A. Lindman, and G. Wahnstöm, Fuel Cells **13**, 19 (2013).
[25]K. D. Kreuer, Solid State Ionics **125**, 333 (2003).
[26]J. Yang, D. Kim, B. Kim, and Y. Kim, submitted to Solid State Ionics (2013).
[27]D. Kim, B. Kim, and Y. Kim, Solid State Ionics **213**, 18 (2012).
[28]P. Lejcek, *Grain Boundary Segregation* (Springer, New York, 2010).

[29]M. C. Payne, M. P. Teter, D. C. Allan, T. A. Arias, and J. D. Joannopoulos, Rev. Mod. Phys., **64**, 1045 (1992).
[30]K. Burke, J. P. Perdew, and M. Ernzerhof, Int. J. Quantum Chem. **61**, 287 (1997).
[31]J. P. Perdew, K. Burke, and M. Ernzerhof, Phys. Rev. Lett. **77**, 3865 (1996).
[32]G. Kresse, Technische Universität at Wien, (1993); G. Kresse and J. Hafner, Phys. Rev. B 47, RC558 (1993); G. Kresse and J. Furthmüller, Comput. Mater. Sci. 6, 15 (1996); G. Kresse and J. Furthmüller, Phys. Rev. B 54, 11169 (1996).
[33]A. Chatterjee and GD. G. Vlachos, J. Computer-Aided Meter Des., **14**, 253 (2007).
[34]A.F. Voter, Introduction to the Kinetic Monte Carlo Method Radiation Effects in Solids, edited by K.E. Sickafus and E.A. Kotomin (Springer, NATO Publishing Unit, Dor-drecht, The Netherlands, 2005) Volume 235: 1-23.
[35]K. A. Fichthorn and W. H. Weinberg, J. Chem. Phys., **95,** 1090 (1991).
[36]D. D. Gillespie, J. Chem. Phys. **115**, 1716 (2001).
[37]J. P. DeVita, L. M. Sander, and P. Smereka. Phys. Rev. B **72**, 205421 (2005).
[38]R. Ciszewski. Senior Thesis. Mount Holyoke College 2012.
[39]J. H. Barnett, http://www.cs.berkeley.edu/~christos/classics/euler.pdf.
[40]Y. Inbar, H. Benyamini, R. Nussinov, and H. J. Wolfson, Bioinformatics **19** (suppl. 1), i158 (2003).
[41]C. W. Marshall, *Applied Graph Theory***, (**Wiley-Interscience, New York, 1971).
[42]G. Chartrand and L. Lesniak. *Graphs and Digraphs*, 2nd ed. Monterey, (Wadsworth, Inc. Monterey, CA, 1986).
[43]M. A. Gomez, D. Shepardson, L. T. Nguyen, and T. Kehinde, *Solid State Ionics* **213**, 8 (2012).
[44]L. C. Freeman, *Social Networks* **1**, 212 (1978).
[45]A. Bavelas, *Human Organization* **7**, 16 (1948).
[46]T. Opsahl, F. Agneessens, and J. Skvoretz, *Social Networks* **32**, 245 (2010).
[47]G. A. Pavlopoulos *et al. BioData Mining* **4**, 10 (2011).
[48]X. Qi, E. Fuller, Q. Wu, Y. Wu, and C. Zhang, *Inform. Sciences.* **194**, 240 (2012).
[49]D. Boley, G. Ranjan, and Z. Zhang, *Linear Algebra Appl.* **435**, 224 (2011).
[50]C. M. Grinstead and J. L. Snell, *Introduction to Proability, Second Revised Edition*, (American Mathematical Society, Providence, RI, 1997).
[51]S. White and P. Smyth, *Proc. 9th ACM SIGKDD Int. Conference on Knowledge Discovery and Data Mining*, **2**, 266 (2003).
[52]M. A. Gomez and F. Liu, submitted to Solid State Ionics (2013).